The Bulk Heterojunction in Organic Photovoltaic, Photodetector, and Photocatalytic Applications

Item Type	Article
Authors	Wadsworth, Andrew; Hamid, Zeinab; Kosco, Jan; Gasparini, Nicola; McCulloch, Iain
Citation	Wadsworth, A., Hamid, Z., Kosco, J., Gasparini, N., & McCulloch, I. (2020). The Bulk Heterojunction in Organic Photovoltaic, Photodetector, and Photocatalytic Applications. Advanced Materials, 2001763. doi:10.1002/adma.202001763
Eprint version	Post-print
DOI	10.1002/adma.202001763
Publisher	Wiley
Journal	Advanced Materials
Rights	Archived with thanks to Advanced Materials
Download date	05/08/2022 07:29:21
Link to Item	http://hdl.handle.net/10754/664558

The Bulk Heterojunction in Organic Photovoltaic, Photodetector and Photocatalytic Applications

Andrew Wadsworth*, Zeinab Hamid, Jan Kosco, Nicola Gasparini, Iain McCulloch*.

Dr. A Wadsworth, Dr. Z. Hamid, Dr. N. Gasparini, Prof. I. McCulloch.
Department of Chemistry and Centre for Plastic Electronics, Imperial College London, Exhibition Road, London, SW7 2AZ, United Kingdom.
E-mail: andrew.wadsworth11@imperial.ac.uk, i.mcculloch@imperial.ac.uk

Dr. J. Kosco, Prof. I. McCulloch
King Abdullah University of Science and Technology (KAUST), KAUST Solar Center (KSC), Thuwal, 23955-6900, Saudi Arabia.

Organic semiconductors require an energetic offset in order to photogenerate free charge carriers efficiently, owing to their inability to effectively screen charges. This is vitally important in order to achieve high power conversion efficiencies in organic solar cells. Early heterojunction-based solar cells were limited to relatively modest efficiencies (< 4%) owing to limitations such as poor exciton dissociation, limited photon harvesting and high recombination losses. The development of the bulk heterojunction (BHJ) has significantly overcome these issues, resulting in dramatic improvements in organic photovoltaic performance, now exceeding 18% power conversion efficiencies. Here we discuss the design and engineering strategies used to develop the optimal bulk heterojunction for solar cell, photodetector and photocatalytic applications. Additionally, we discuss the thermodynamic driving forces in the creation and stability of the bulk heterojunction, along with underlying photophysics in these blends. Finally, we discuss new opportunities to apply the knowledge accrued from BHJ solar cells to generate free charges for use in promising new applications.

1. The Evolution of the Bulk Heterojunction

Organic semiconducting materials have been exploited extensively in energy conversion and electronic applications for over two decades, resulting in significant advances in both material

design and device engineering. In organic photovoltaics (OPVs), developments, such as the optimization of the device architecture, strategic design of the organic semiconductors and control of the mixing and phase separation of two or more of these semiconductor components have drastically raised the power conversion efficiency (PCE) that can be achieved from less than 1% in 1976 to over 18% in 2020.[1,2] Similarly, significant improvements have also been observed in organic light emitting diode (OLED) and field effect transistor (OFET) applications.[3,4] More recently, a number of other applications of organic semiconductors are emerging, such as organic electrochemical transistors (OECTs), organic photodetectors (OPDs) and organic semiconducting photocatalysts to drive chemical reactions.[5-9]
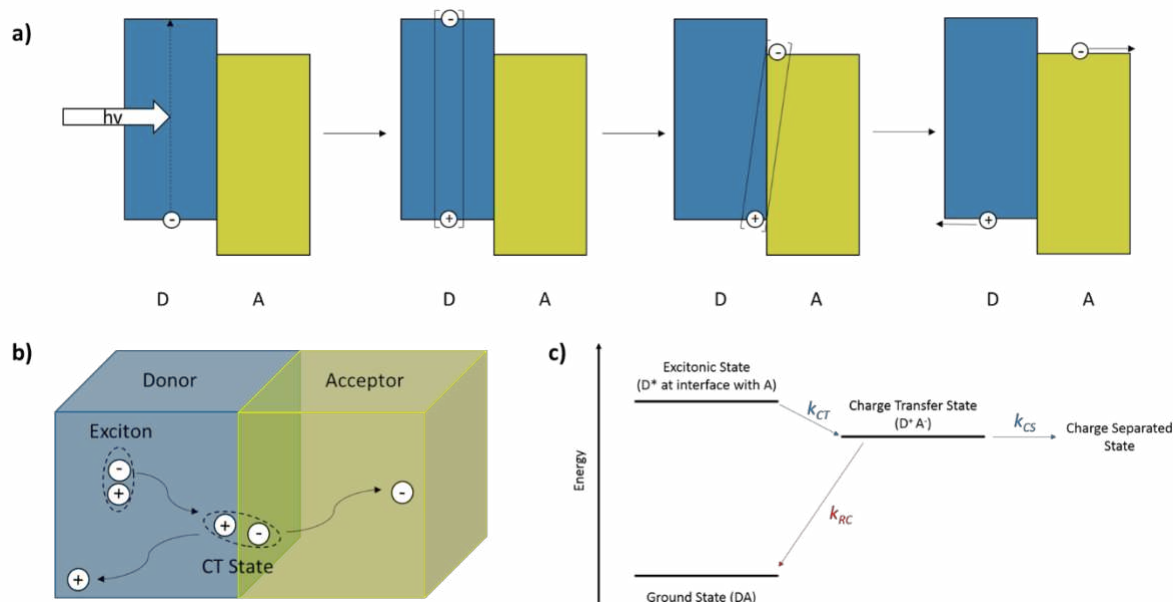
Figure 1. (a) Schematic of the process of light absorption, exciton formation and charge separation in organic semiconductors with a type-II offset, (b) Schematic illustrating the diffusion of excitons to the donor-acceptor interface, formation of the charge transfer state and eventual migration of free charges away from the interface upon charge separation and (c) energy level diagram summarizing the ground, excitonic, charge transfer and charge separated states in a an organic semiconductor heterojunction.

Semiconducting materials possess a number of advantages over their inorganic counterparts: (i) facile tuning of the frontier energy levels and structural properties, which allows control of the photon absorption/emission, solid-state packing/morphology and the ability to accept/donate charge carriers, (ii) the ability to solution process which facilitates a range of

high throughput fabrication processes and (iii) the opportunity to integrate with flexible materials and substrates for devices with a variety of form factors. However, a number of the inherent properties of organic semiconductors present potential drawbacks that have had to be overcome in order for efficient organic electronic devices to be realized. When an organic semiconductor absorbs a photon of light, with energy greater than or equal to its bandgap (E_g), an electron is promoted from the highest occupied molecular orbital (HOMO) to the lowest unoccupied molecular orbital (LUMO), leaving a positively charged void, referred to as a hole, in its place. This is shown in **Figure 1a**. The comparatively low dielectric constant of organic semiconductors render them unable to effectively screen charges. This results in the existence of coulombically bound electron-hole pairs (known as excitons), upon photoexcitation, in comparison to the free charges formed in inorganic semiconductors at room temperature. This inability to create free charge carriers was apparent in some of the earliest reported OPVs, which consisted of a single organic semiconducting material sandwiched between two electrodes. These initial organic solar cells were unable to generate significant photocurrents due to the fact that very few of the excitons formed, upon the organic semiconductor absorbing incident light, were able to split into free charges.[1,10] As such, it became clear that an additional driving force would be required in order to drive the scission of these excitons into free photogenerated charges, which could be subsequently collected at the device electrodes. The approach adopted in order to achieve this was the inclusion of a second organic semiconductor material, with shifted frontier molecular orbitals (FMOs), such that a type-II offset exists. The semiconductor with more shallow lying FMOs is known as the electron donor and the semiconductor with deeper FMOs is known as the electron acceptor. Upon the absorption of light in the electron donor material, an exciton is formed, which must then reach an interface with the electron acceptor material. Once the exciton reaches the interface, it is thermodynamically more favourable for the electron to be situated in the LUMO of the electron acceptor material and the hole to remain in the HOMO of the electron donor material. Whilst this electron-hole pair are

still coulombically bound and located at the donor/acceptor interface, this species is often referred to as an intermolecular charge transfer (CT) state. From this point, there are two possible fates of the electron-hole pair: (i) the exciton binding energy can be overcome, via a thermodynamic driving force, resulting in spatially separated free charge carriers (known as the charge separated state) or (ii) the electron and hole recombine resulting in a ground-state system, where no free charge carriers are generated. This is illustrated in Figure 1b and 1c. With this in mind, it is clear that in order to produce the greatest number of free charge carriers upon illumination, one must maximize the rates of charge transfer and charge separation (k_{CT} and k_{CS} respectively), whilst minimizing the rate of recombination (k_{RC}).

As a result of the relatively high exciton binding energy in organic semiconductors (0.3 – 0.5 eV), a large driving force is needed to separate the exciton into free charge carriers.[11,12] Until recently, it was widely considered that the LUMO-LUMO or HOMO-HOMO offsets (ΔE_{LUMO} and ΔE_{HOMO} respectively) between the electron donor and electron acceptor materials must be at least 0.3 eV in order to overcome this exciton binding energy, allowing electron and hole transfer (ET and HT respectively) across the interface.[13] As such, most OPVs made use of donor and acceptor materials with ≥ 0.3 eV offset of their respective FMOs. This limits the output photovoltages that can be achieved, since the open circuit voltage (V_{OC}) is related to the difference in energy between the electron donor's HOMO and electron acceptor's LUMO level. In recent times, however, there have been a number of examples of OPV systems in which ΔE_{LUMO} was less than 0.3 eV.[14-16] In many cases, these devices were still able to produce state-of-the-art photovoltages, whilst still retaining competitive PCEs, leading researchers to reconsider this empirical ΔE_{LUMO} limit.[15,16] There have since been suggestions that a number of other physical phenomena occur at the interface, which may aid the CT state to separate into free charges, thereby lowering the driving force required to overcome the exciton binding energy.[17] The spontaneity of a process is dictated by the Gibbs free energy, therefore both enthalpic and entropic contributions must be considered. Firstly, upon the formation of a charge

transfer state, a dipole often forms at the interface. This dipole can arise for a number of reasons, such as a difference in polarizability of the donor and acceptor, the breaking of symmetry or charge redistribution.[18] This interfacial dipole can act as an electronic energy gradient, which can assist exciton separation into free charges. Moreover, the lack of stabilising local packing or mixed phases at the interface leads to higher FMO energy levels, and an energy cascade arises.[19] This can result in an electronic energy gradient that favours free charges moving away from the interface, to a lower energy region. Often, there can be electron delocalization that favours a long range CT state after initial excitation.[20] Should this delocalisation happen very quickly, it can be followed by charge localisation with sufficient spatial separation of the hole and electron such that it favours dissociation. Another consideration is that the three-dimensional phase space for electrons and holes is greater, the farther from the two-dimensional donor/acceptor interface, acting as an entropic driving force for exciton splitting.[21] In totality, the aforementioned effects result in a free-energy gradient that can assist exciton scission, even if the ΔE_{LUMO} (or ΔE_{HOMO}) are smaller than 0.3 eV.
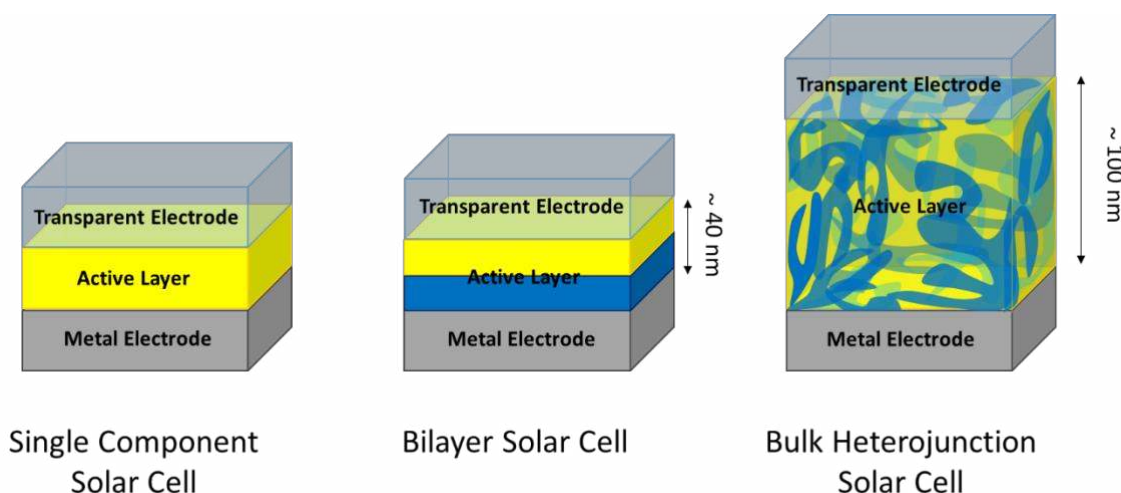

Figure 2. Schematic of single component, bilayer and bulk heterojunction organic solar cells.

Since an energetic driving force, given by a type-II offset at the interface with a second organic semiconductor, is needed in order to split excitons into free charges, it is imperative that excitons reach an interface before they can relax back to the ground state. The distance that an

exciton can travel before this relaxation occurs is known as the exciton diffusion length (L_D). Whilst there is some debate about this typical distance, most estimated values of L_D in organic semiconductors are between 5 and 10 nm.[22,23] Therefore, in order to minimize the number of excitons that can relax back to the ground state, they must be in close proximity (tens of nm) to an interface. With this consideration in mind, early heterojunction solar cells made use of two sequentially deposited thin layers (10-20 nm) of an electron donor and electron acceptor material sandwiched between a cathode and anode to extract the charges. This device configuration is known as a bilayer solar cell, and is shown in **Figure 2**. This shift from single component organic solar cells to bilayer cells proved to be very effective, with vast improvements in the PCE from ~0.1 % achieved in single component devices to 1-4 % in bilayer cells, summarized in **Table 1**. This was manifested mainly in dramatic improvements in short circuit photocurrent density (J_{SC}) and fill factor (FF), as the excitons formed from photoexcitation were able to split into free charge carriers more readily. The first reported OPV bilayer cell made use of copper phthalocyanine (CuPc) and a perylene derivative (PV), sequentially deposited by sublimation, producing a then-record PCE of 1%.[24] Further attempts to improve bilayer solar cells were made with the modification of the CuPc structure, instead using a tri-substituted boron subpthalocyanine chloride (SubPc), in combination with fullerene (C_{60}) to increase the band offset, significantly increasing the V_{OC}.[25] This allowed PCEs of up to 2.1% to be achieved, although later optimization of the active layer deposition rate afforded PCEs of up to 4%.[26] This improvement in performance was attributed to preferential changes in molecular packing that further increased the V_{OC}, by increasing the energy between the SubPc HOMO and C_{60} LUMO, and improved FF by reducing the energy barrier to the anode. Attempts to design organic polymer-containing bilayer solar cells were also made, in order to achieve solution-processed devices.[27] However, such devices were unable to exceed efficiencies of 2% and often required stringent optimization of charge selective interlayers to maximize V_{OC}, and therefore PCE.

Table 1. Summary of the key photovoltaic parameters of notable bilayer organic solar cells.

Active Layer	J_{SC} [mA cm^{-2}]	V_{OC} [V]	FF	PCE [%]	Processing	Reference
CuPc:PV	2.3	0.45	0.65	0.95	Sublimation	[24]
SubPc:C$_{60}$	3.4	0.97	0.57	2.1	Sublimation	[25]
SubPc:C$_{60}$	5.6	1.02	0.66	4.0	Sublimation	[26]
P3HT:IDSe-DFBT	3.7	1.13	0.49	2.0	Solution Processing	[27]

Despite the improvements made in device performance upon adopting a bilayer configuration, there were also a number of drawbacks associated with this approach. Firstly, in order to ensure that excitons are able to reach an interface before relaxation, the layers of organic semiconductor are relatively thin in a bilayer cell. This results in the total thickness of the active layer being around 20-40 nm. Although organic semiconductors are typically strongly absorbing in the visible region of the solar spectrum, such thin active layers are not able to absorb all of the incident photons reaching a device, limiting the photocurrent and quantum efficiencies that devices can achieve.[28] Attempts were made to produce much thicker bilayer devices, such that the transmission of incident photons through the device was minimized, however they suffered from significant losses due to exciton recombination, resulting in decreased PCE in devices.[29] Another significant issue with bilayer cells is the limitation of donor and acceptor materials that can be used. As the donor and acceptor layers are sequentially deposited, one on top of the other, care is needed to avoid damaging the first layer when the second is deposited, particularly when solution processing is used to deposit the active layer, thus requiring solvent orthogonality between the two layers. This can be avoided by using sublimation or vacuum-based vapour deposition to deposit the organic semiconductors, although these techniques have more challenges to be scalable. Another strategy is to crosslink the first layer after it has been deposited, thus rendering it more robust upon deposition of the second layer.[30] However, crosslinking has been known to negatively impact the charge

transport properties of organic semiconductors, disrupting ordered packing of polymers and small molecules, thereby reducing the photocurrent and increasing recombination in devices.[31] In order to resolve the above issues, further evolution of the heterojunction solar cell was required. This was achieved by the bulk heterojunction (BHJ) solar cell, where the planar interface of a bilayer cell was replaced with an interface dispersed throughout the bulk of the active layer. In order to ensure that the majority of excitons are able to reach an interface prior to relaxation, an interpenetrating network of donor and acceptor domains on the length scale of 10-20 nm is required, in addition to the presence of contiguous percolation pathways of donor- and acceptor-rich domains that allow the collection of free charge carriers at the device electrodes. This is illustrated in Figure 2. The presence of interfaces throughout the active layer allows thicker devices to be fabricated, without substantially increasing losses due to relaxation and recombination. Consequently, BHJ solar cells have been able to harvest a greater fraction of incident photons than their bilayer counterparts, resulting in improved photocurrents. This has led to drastic improvements in device performance, in comparison to single component and bilayer solar cells, with early BHJ solar cells attaining PCEs as high as 3-5%, but with improvements made in the chemical design of donor and acceptor materials this has now been able to reach over 18%, highlighting the success of the bulk heterojunction approach.[2,32,33] Moreover, the BHJ active layer is predominantly formed by depositing a solution containing a blend of both the donor and acceptor materials. Hence, in BHJ solar cells, solvent orthogonality of the donor and acceptor components is not required; opening the door to a vast range of possible material combinations.

The careful selection of the correct donor and acceptor materials are key when designing a new BHJ solar cell, with attention needed to both the optoelectronic and structural properties of each organic semiconductor. As discussed above, the energy of the HOMO and LUMO of the donor and acceptor must be considered to ensure a type-II offset, but also the E_g and absorption profiles of the donor and acceptor should be complementary, such that the maximum fraction

of incident photons in the solar spectrum can be utilized. Control of the phase separation is also of great importance in BHJ solar cells, ensuring that the optimal interpenetrating network of donor and acceptor domains on the nanoscale is formed. Generally, this is dictated by the relative crystallinity and miscibility of the donor and acceptor materials. A fine balance exists between having enough crystallinity, or structural order, in each component for efficient charge transport with minimal trapping, whilst retaining adequate miscibility of the donor and acceptor to ensure nanoscale phase separation. This can be achieved by using a combination of the following approaches: (i) judicious selection of complementary donor and acceptor materials to fall within the window of optimal miscibility, (ii) modulation of the crystallinity and solid-state order of each organic semiconductor via chemical design and (iii) optimization of the donor:acceptor ratio and processing conditions. In order to control the local and extended order in organic semiconductors, the conjugated backbone planarity and steric interactions between polymer chains/molecules must be manipulated. Among the most commonly used strategies in order to do this is the use of alkyl chain optimisation. For example, the addition of branching in the solubilizing side chains can inhibit the ability of polymer (or small molecule) conjugated backbones to aggregate with neighbouring backbones, thereby reducing the order in the semiconductor and rendering it more likely to mix with the second component.[34,35] On the other hand, if a blend is too intimately mixed, whereby no clear donor- or acceptor-rich domains form, reducing the density of solubilizing sidechains, and employing straight chain alkyl groups that are able to assemble and crystallise can improve the order of a semiconductor, leading to a lower probability of its local order being disrupted by the second component. Another tactic that is often employed to reduce the order, and therefore improve the miscibility, in planar small molecules is to promote steric twisting along the aromatic conjugated unit.[36] Similar to the use of branched side chains, the additional steric interactions of these twisted 3D structures can impede the close π-π stacking of conjugated backbones, reducing the ability to pack in an ordered fashion. In some cases, the donor:acceptor ratio can be altered in order to encourage

phase separation and therefore the formation of distinct donor:rich and acceptor rich domains. This is often required in blends that make use of relatively amorphous polymers, or those that contain fullerene acceptors, where a small molecule component often becomes molecularly mixed within the polymer phase.[37] It has been shown that increasing the amount of the small molecule, relative to the polymer, enables the formation of small molecule rich domains and the presence of percolation pathways in the active layer.[38]

At first, it was thought that an ideal BHJ would only contain pure donor and pure acceptor phases, providing the interface needed for exciton scission, whilst retaining local order in both the donor and acceptor to facilitate efficient hole and electron transport, respectively. Moreover, pure phases reduce the probability of non-geminate recombination of free charge carriers as they are transported to the electrodes to be collected. However, many state-of-the-art BHJ solar cells contain both pure and mixed domains in the active layer, indicating that these mixed domains are in fact advantageous for charge separation processes.[39,40] As noted above, the presence of mixed phases and structural disorder at the donor/acceptor interface can create an electronic energy gradient, which is highest in energy at the interface and subsequently decreases with increasing distance from the interface, which facilitates excitons splitting into free charges. Additionally, there is some suggestion that the presence of both pure and mixed phases provide an energy cascade that minimizes geminate recombination.[41] The presence of an energetic barrier ensures that once a charge carrier crosses from a mixed phase to an aggregated pure phase it is very unlikely to cross back in the other direction. It is important, though, to retain some pure donor and acceptor phases to ensure facile transport of free charge carriers to the electrodes and reduce the probability that free holes and electrons encounter one another prior to collection, which can result in non-geminate recombination.

Whilst the main focus of OPV research in the past 20 years has been maximizing the PCE that devices can achieve, another vital milestone is the development of stable organic solar cells. If OPV technologies are ever to be realized as commercial products, the inherent photostability

of the organic semiconductors used, and the morphological stability of their BHJ blends, must be significantly improved to yield device lifetimes of over 10 years.[42] Issues of photostability can be combatted by the encapsulation of devices, to minimize the occurrence of photo-oxidation and reducing light-induced traps via the replacement of fullerenes, which can undergo photodimerization, for more stable non-fullerene alternatives.[43,44] However, a remaining concern is the morphological stability of the BHJ. Many of the most promising OPV devices, reported to date, exhibit poor morphological stability as a result of demixing of the donor and acceptor components over time. Judicial selection of complementary donor and acceptor components, by considering their miscibility with one another, is needed in order to avoid the demixing or spinodal decomposition of a blend. If the donor and acceptor have relatively poor miscibility, or are able to effectively diffuse through the blend over time, a nanoscale blend of the two components is thermodynamically unfavourable.[45,46] Thus, large scale demixing can occur over time, resulting in the loss of the optimized blend morphology and larger micrometre to millimetre sized domains can be formed. Consequently, many of the excitons formed upon photoexcitation are no longer able to reach an interface within the L_D, resulting in substantial geminate recombination losses and poor photocurrent generation in devices.

2. Progress in Semiconductor Design and Device Engineering for Improved Bulk Heterojunction OPVs

2.1. Polymer:Fullerene Blends in Bulk Heterojunction Solar Cells

The most common selection of materials in BHJ solar cells, until recently, was a polymer donor used in combination with a fullerene-based acceptor. There are several reasons for the widespread popularity of this polymer/fullerene combination, such as the excellent film-forming properties from solution processing, the ability to form interpenetrating nanoscale donor and acceptor domains and the excellent electron transport properties afforded by fullerenes.[47,48] It should be noted however that the fullerene acceptors absorb poorly in the

visible region of the solar spectrum, where the incident solar flux is greatest, therefore photoexcitation occurs mainly in the donor material.[32] The excitons formed in the polymer donor must then migrate to an interface with the fullerene phase in order to split the exciton, donating electrons to the fullerenes and leaving free holes in the polymer donor. This is known as channel-I photoexcitation.

Table 2. Summary of the key photovoltaic parameters of notable polymer:fullerene BHJ organic solar cells.

Active Layer	J_{SC} [mA cm^{-2}]	V_{OC} [V]	FF	PCE [%]	Additive	Reference
MEH-PPV:PC$_{61}$BM	2.7	0.76	0.50	1.3	n/a	[49]
P3HT:PC$_{61}$BM	9.5	0.63	0.68	5.1	n/a	[33]
P3HT:IC$_{70}$BA	11.4	0.87	0.75	7.4	1-chloronapthalene (3%)	[55]
PCDTBT:PC$_{71}$BM	10.6	0.88	0.66	6.1	n/a	[56]
PTB7-Th:PC$_{71}$BM	17.4	0.83	0.74	10.7	1,8-diiodooctane (3%)	[57]
PffBT4T-2OD:PC$_{71}$BM	18.8	0.77	0.75	10.9	1,8-diiodooctane (3%)	[58]

A number of the notable polymer/fullerene BHJ solar cells are summarized in **Table 2**, charting the significant improvement in device performance made over the past 30 years. Some of the earliest BHJ devices made use of poly[2-methoxy-5-(2-ethylhexyloxy)-1,4-phenylenevinylene] (MEH-PPV) as the polymer donor, in combination with a soluble fullerene derivative known as phenyl-C$_{61}$ butyric acid methyl ester (PC$_{61}$BM), in a 1:4 weight ratio. Devices were only able to attain PCEs of up to 1.3%, as they were limited by relatively low J_{SC}, due to the wide bandgap of the poly(phenylvinylene)s (~2.2 eV).[49] This limits the absorption of photons to approximately 600 nm, leaving a large lower energy fraction of this visible solar flux unused. Moreover, the hole mobility of the PPV derivatives was shown to be an order of magnitude lower than the electron mobility of fullerenes; an imbalance in the charge carrier mobilities that can lead to increased recombination in devices.[50] As an alternative to the PPV polymers, poly(3-alkylthiophene)s (P3ATs) were then selected, which are simple thiophene

homopolymers with an alkyl chain at the 3 position to confer improved solubility and device processing. Among the most successful of these was regioregular poly(3-hexylthiophene) (P3HT), a polymer that can form highly ordered microcrystalline lamella.[51] When blended with $PC_{61}BM$, devices afforded PCEs of up to 5%, owing to the greater hole mobility of the ordered P3HT and consequent reduction in recombination.[33] Additionally, the improved crystalline order of the P3HT affords a narrower bandgap than the PPV derivatives (~1.9 eV), leading to improved photon absorption and greater device photocurrents. It has been shown extensively that thermal annealing of the $P3HT:PC_{61}BM$ blend can improve the device PCE.[52] This allows the P3HT to recrystallize into more ordered packing structures and reduces the density of defects at the interface, thereby improving the hole mobility. However, the large voltage losses in $P3HT/PC_{61}BM$ cells severely limited the V_{OC} that could be achieved with this blend to 0.67 V.[53] Fullerene modifications, including the use of bisadducts to raise the LUMO and the replacement of the highly symmetric C_{60} unit with its C_{70} analogue, to improve its photon harvesting capabilities, were utilized in the design of indene-C_{70} bisadduct ($IC_{70}BA$). When combined with P3HT, has been shown to reach device PCEs exceeding 6.7%.[54] With the formation of an improved interpenetrating network, by using the high boiling 1,8-diiodooctane (DIO) additive, efficiencies were able to reach 7.4%.[55] The effect of utilizing solvent additives and co-solvents on blend morphology and device performance is discussed in greater detail below. Another promising donor polymer that has been used in combination with the fullerene acceptors is poly[N-9′-heptadecanyl-2,7-carbazole-alt-5,5-(4′,7′-di-2-thienyl-2′,1′,3′-benzothiadiazole)] (PCDTBT). When blended with the C_{71} analogue of $PC_{61}BM$, phenyl-C_{71} butyric acid methyl ester ($PC_{71}BM$), in BHJ solar cells, devices were able to reach efficiencies of over 6%.[56] The use of 1,2-dichlorobenzene was shown to allow the formation of percolating PCDTBT and $PC_{71}BM$ pathways on the nanoscale, whilst other solvents, such as chloroform and 1-chlorobenzene, produced significantly larger domains. The preferable morphology in 1,2-dichlorobenzene processed devices afforded improved FF and J_{SC}, a result

of more effective charge transport and collection, leading to greater efficiencies than devices processed from the other solvents.

Later advances in the chemical design of so-called donor-acceptor copolymers, which make use of push-pull hybridization from conjugation of electron-rich and electron poor alternating repeat units, led to the possibility to produce much narrower bandgap donor polymers. As such, drastic improvement in the photon harvesting capabilities of BHJ solar cells was possible, and photocurrents exceeding 10 mA cm-2 were achievable. A notable example of this was with PTB7-Th.[57] The improved photon absorption of PTB7-Th, in comparison to many of the aforementioned polymers, led to substantially greater Jsc in devices (> 17 mA cm-2) and resulted in PCEs exceeding 10% in devices, despite the polymer being relatively amorphous in nature.. It has been suggested that the alkylthienyl solubilizing groups can assist the self-assembly and ordering of the polymer, featuring two-dimensional conjugation and improved π-π stacking between polymer chains. One of the more recent significant developments made in polymer:fullerene BHJ solar cells was the design of a relatively crystalline donor-acceptor copolymer, poly[(5,6-difluoro-2,1,3-benzothiadiazol-4,7-diyl)-alt-(3,3'''-di(2-octyldodecyl)-2,2',5',2'',5'',2'''-quaterthiophen-5,5'''-diyl)] (PffBT4T-2OD), an alkylated quaterthiophene copolymerized with a difluorobenzothiadiazole. The strong push-pull hybridization and planar polymer backbone afford a narrow bandgap (~1.6 eV), similar to PTB7-Th, whilst careful selection of the alkyl chain length and branching point led to strong aggregation, as evidenced by significant temperature-dependent thin film absorption properties. In a series of analogues of PffBT4T-2OD, it was shown that careful control of the aggregation, by alkyl chain engineering, led to preferential phase separation on the nanoscale and high purity of polymer domains. When blended with PC71BM, and processed from 1-chlorobenzene, with DIO as an additive, devices were able to approach a PCE of 11%.[58] Later work presented another analogue, PffBT4T-C9,C13, which demonstrated further improvements in the efficiency of devices with PC71BM by employing a non-chlorinated solvent (1,2,4-trimethylbenzene) with

1-phenylnapthalene as an additive. Efficiencies of 11.3% were achieved through an improved device morphology, highlighting the importance of controlling aggregation and miscibility of the two components in a BHJ solar cell.[59]

The choice of solvent and the use of additives provide the opportunity to control the microstructure in BHJs, and have contributed significantly to the advances made in optimizing the BHJ over the last two decades. Aromatic, and chlorinated, solvents are among the most popular in the deposition of organic BHJs, owing to their high degree of interaction with relatively insoluble conjugated polymer chains and their relatively high boiling points, which allow reorganization to favourable packing. The high boiling additives, such as DIO and CN, reduce the viscosity of the solution and increases its wettability. Moreover, as noted above, solutions with higher boiling points offer lower drying rates that lead to better mixing and reordering of the layer is possible. These additives are particularly useful in polymer:fullerene blends as they ensure that the fullerenes remain well dissolved allowing a better mixture with the polymer and avoiding the formation of larger scale agglomerates during deposition of the BHJ.[60-62]

There are a number of common features in polymer:fullerene solar cells that should be noted. Firstly, the blend ratio is usually much richer in a fullerene acceptor, often as high as 1:4 (polymer:fullerene); there are many studies that have investigated the effects of blend composition on morphology and device performance, and the inherent molecular mixing often displayed in fullerenes necessitates fullerene-rich blends in order to produce the percolation pathways for high performance devices. Secondly, polymer:fullerene blends often require the use of a high boiling additive, such as DIO, in order to control the phase separation to form nanoscale domains. Finally, polymer:fullerene solar cells often display poor morphological stability owing to the aggregation of fullerenes over time, and migration to the device electrodes, residual solvent additives are also known to accelerate this process.[63,64]

2.2. The Development of Nonfullerene Acceptors for High-Performance Bulk Heterojunction Solar Cells

Despite the success of the fullerene acceptors, a number of drawbacks exist; such as their poor optical absorption, and their strong tendency to aggregate, and sometimes dimerize, over time. Their relatively low extinction coefficients and absorption predominantly in the UV region of the solar spectrum, restricts polymer/fullerene solar cells to operate predominantly with channel-I photoexcitation. However, channel-II excitation (where the acceptor absorbs a photon, creating an exciton) can also be exploited with acceptors possessing much stronger optical absorption, usually in the visible region. This can greatly improve the photocurrents attained in BHJ solar cells. The poor morphological stability of fullerenes can prevent long term retention of the required nanostructure for high performance BHJ solar cells, with large microscale domains and device delamination evolving over time, as discussed above. The inability to tune the FMO energy levels in fullerenes also place significant limitations to the V_{OC} that can be achieved in devices, with very few examples exceeding 0.8 V. These issues prompted significant research focus on the development of alternative electron acceptors, known as non-fullerene acceptors (NFAs), which can be either polymers or small molecules. In particular, chemical modification has allowed greater control over the BHJ morphology formed, resulting in significant improvements in OPV performance. A number of notable NFA solar cells are summarized in **Table 3**.

Table 3. Summary of the key photovoltaic parameters of notable polymer:nonfullerene BHJ organic solar cells.

Active Layer	J_{SC} [mA cm^{-2}]	V_{OC} [V]	FF	PCE [%]	Additive	Reference
PTB7-Th:PDI	4.9	0.81	0.60	2.4	1,8-diiodooctane (0.5%)	[67]
PTB7-Th:Ta-PDI	17.1	0.78	0.69	9.2	n/a	[69]
P3HT:FBR	8.0	0.82	0.63	4.1	n/a	[70]
P3HT:O-IDTBR	14.6	0.73	0.66	7.0	n/a	[72]
PTB7-Th:EH-IDTBR	18.5	1.03	0.63	12.0	n/a	[73]

PBDB-T:ITIC	16.8	0.90	0.74	11.2	1,8-diiodooctane (0.5%)	[78]
PBDB-T-SF:IT-4F	20.9	0.88	0.71	13.1	1,8-diiodooctane (0.5%)	[78]
PM6:Y6	25.2	0.82	0.76	15.7	1-chloronaphthalene (0.5%)	[81]
D18:Y6	27.7	0.86	0.77	18.2	n/a	[84]

Early examples of NFAs were highly planar, electron deficient small molecules based on the perylene diimide (PDI) structure.[65,66] These molecules have a large π-conjugated area, to allow effective overlap of the FMOs of neighbouring molecules, resulting in good electron transport properties. However, the planar π-conjugated structures also significantly increase the tendency of the PDI molecules to self-aggregate, resulting in microscale phase separation when blended with most donors.[66] As a result, these early PDI acceptors were limited to efficiencies of less than 3% in PTB7-Th:PDI solar cells, with relatively low FF and J_{SC} (0.52 and 4.8 mA cm$_{-2}$ respectively).[67] It became apparent that the strong aggregation tendency of PDIs limited their BHJ device performance, particularly when blended with polymer donors. Subsequent design strategies of PDI-based NFAs therefore focused on supressing their strong aggregation tendency, usually by synthesizing twisted PDI dimers or trimers. Examples include h-di-PDI, a twisted imide-linked PDI dimer, where the two PDI units were oriented perpendicular to one another, and Ta-PDI, in which three PDI units were linked at the imide position to a central triazine core.[68,69] The highly twisted structures produced in these PDI dimers and trimers effectively suppressed the strong aggregation tendency of PDIs. In BHJ solar cells with PTB7-Th as the donor, both were able to form nanoscale blend morphologies, reflected in their relatively high FF and J_{SC}, ultimately resulting in maximum PCEs of 6.4% and 9.2% for h-di-PDI and Ta-PDI respectively.[68,69]

Another design approach to NFAs made use of so called "acceptor-donor-acceptor" (A-D-A) structures, rather than large planar π-conjugated systems, where "donor" refers to electron rich

segment of the conjugated system, and "acceptor" refers to an electron withdrawing segment, with respect to the electron rich segment. These were designed to be modular, for facile tuning of the optoelectronic and structural properties. Particularly, the A-D-A structure makes use of push-pull hybridization to ensure the absorption at lower energies of the solar spectrum, whilst leaving the acceptor moieties (where the LUMO will predominantly lie) on the periphery of the molecule to ensure that electrons can efficiently hop between acceptor molecules. An early example of an A-D-A NFAs was FBR, an acceptor in which an alkylated fluorene core was flanked on either side by benzothiadiazole and rhodanine units. When blended with P3HT, FBR devices were able to reach efficiencies of 4% and displayed significantly improved thermal stability over P3HT:PC$_{61}$BM blends.[70] The phenyl-phenyl link between the fluorene and benzothiadiazole units lead to a backbone twist to avoid the steric clash of hydrogen atoms adjacent to the linkage, this backbone twist suppresses excessive aggregation between FBR molecules, affording the improved stability. However, the amorphous morphology and miscible nature of FBR, led to molecular mixing rather than forming distinct acceptor domains on the nanoscale. This was addressed with the development of alkylated indacenodithiophene-based analogue, IDTBR, in which the phenyl-phenyl link was replace with the more coplanar thienyl-phenyl link. The reduced steric interactions in IDTBR lead to a planar backbone in the NFA. Consequently, this affords a narrower bandgap, due to greater effective conjugation, and a greater aggregation tendency, resulting in a more favourable blend morphology in BHJ devices with P3HT.[71] This improved morphology, and complementary absorption to P3HT, manifest in improved J$_{SC}$ and FF in comparison to FBR, achieving a maximum PCE of 7%.[72] Later reports demonstrated the versatility of IDTBR, when paired with the relatively amorphous PTB7-Th, at a 1:1 weight ratio, efficiencies of 12% could be attained, despite the relatively low energetic offsets and similar absorption spectrum with PTB7-Th.[73] Among the most common A-D-A NFAs, is ITIC and its subsequent analogues.[74-76] ITIC consists of an indacenodithienothiophene core flanked on either side by a vinyl-linked dicyanovinyl indanone

(DCI) unit, resulting in a relatively similar bandgap to IDTBR. One notable difference, however, was the presence of phenylalkyl side chains, which has been shown to reduce the ability of small molecules to pack closely.[77] In BHJ solar cells, the PTB7-Th:ITIC blend was able to achieve up to 6.8% PCE, which was state-of-the-art at the time it was reported.[74] The efficiency achievable in ITIC-based solar cells was later improved by pairing it with a wide bandgap donor polymer, known as PBDB-T, which provided greater photocurrent via complementary absorption of donor and acceptor, and more balanced charge carrier mobilities, culminating in PCEs of over 11%.[78] A number of modifications have been made to ITIC-based NFAs, the most notable of which have involved the addition of functional groups to the phenyl ring of the DCI endgroups.[78-80] IT-4F made use of the addition of fluorine atoms to the DCI unit in order to improve intermolecular interactions between NFA molecules and therefore the electron mobility of the NFA.. Overall, a substantial improvement in the device photocurrent was observed and PCEs of over 13% were achieved for the first time in single junction organic solar cells.[78] More recently, a novel A-D-A-D-A type NFA has accelerated the field of BHJ solar cells substantially. Y6, consists of a bent π-conjugated core, flanked on either side by the fluorinated DCI units that were used previously in IT-4F. The first reported devices of Y6, when blended with PM6, which is another fluorinated derivative of PBDB-T, yielded PCEs of up to 15.7%.[81] It has been suggested that this significant improvement in device performance over all other NFAs is related to the narrow bandgap (1.33 eV), formation of ~40 nm domains in the blend and the preservation of endgroup packing in Y6, even upon blending with the donor polymer. Particularly, the molecular packing gives very high electron mobilities in the BHJ blend, so when coupled with improved photon harvesting, it is possible to achieve impressive J_{SC} and FF (25 mA cm$_{-2}$ and 0.76 respectively). It has also been shown that the molecular design minimizes the possibility for molecular disorder in Y6, with a single conformational isomer present, even upon blending with a polymer, a feature not commonly seen in NFAs.[82] Recent optimization of the interfacial layers and tuning of the donor polymer structure (D18) has led

to PCEs of 17-18% now possible for the Y6-based blends, highlighting such systems as standout candidates for further modification in the pursuit of ever higher device efficiencies.[83,84] A number of the key donor and acceptor materials used in bulk heterojunction OPVs are summarized in **Figure 3**.
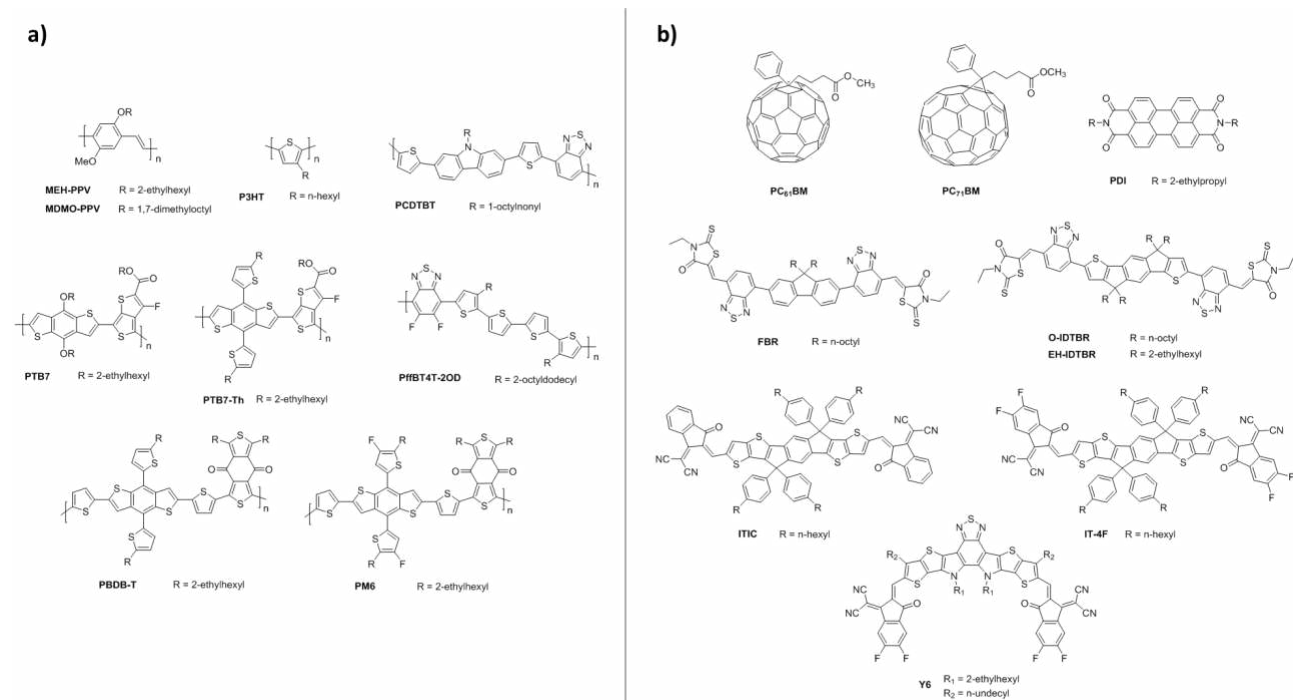

Figure 3. Chemical structures of commonly used (a) electron donor materials and (b) electron acceptor materials for bulk heterojunction solar cells.

All-polymer BHJ solar cells have also been investigated extensively, but do not present competitive performances in comparison to polymer:small molecule OPV devices. The main reason for this is that it is often challenging to optimize the morphology of all-polymer bulk heterojunctions; a result of the lack of an entropic driving force in the mixing of two polymeric components. Despite this, all-polymer BHJ solar cells can offer advantages not afforded by the small molecule acceptors, such as the opportunity for improved morphological stability owing to entanglement and the much slower diffusion of polymers in a blend.[85] A common design motif in these acceptor polymers is the presence of a naphthalene diimide (NDI) moiety. The most thoroughly studied polymer NFA is P(NDI2OD-T2) and its analogues; consisting of an NDI unit, with long, branched 2-octyldodecyl solubilizing chains, copolymerized with

bithiophene.[86] Early research into this acceptor polymer, blended with P3HT, was only able to achieve 0.2% PCE, as the unfavourable polymer mixing resulted in unfavourably large domains (> 200 nm).[87] This was later improved to 1.4% PCE, through the use of solvents with large and polarisable aromatic cores, as it promoted the formation of smaller domains in the BHJ.[88] Through judicious selection of the donor polymer, it is possible to control the blend morphology, creating domains on the order of tens of nm, and thus the achievement of more competitive PCEs (4-10%).[89-92] To date, the best performing blend in an all-polymer solar cell makes use of P(NDI2OD-T2) blended with a wide bandgap benzodithiophene based polymer with siloxane terminated side chains (PTzBI-Si) and can afford a maximum PCE of 10.1%.[92] The authors noted that the fact that both polymers retained the same preferential face-on packing orientations in when blended together was beneficial for charge transport and likely contributed to the high photovoltaic performance. Whilst significant progress has been made in all-polymer solar cells, with careful selection of the two polymer components and solvent processing optimization, the difficulty in optimizing blend morphology, and the substantially lower device performance at present, render them a less promising opportunity in BHJ solar cells.

Another BHJ strategy makes use of small molecules both as the electron donor and acceptor materials (SM:SM solar cells). The chemical composition of small molecules is more precise than the range of molecular weights present in a typical polymer, which makes the batch to batch consistency of the materials more reliable. A major drawback of all-small molecule solar cells, however, is their poorer film-forming properties and the difficulty in controlling the nanoscale blend morphology. Early examples of SM:SM solar cells paired the fullerene acceptors discussed above, with donors such as BTR, a liquid crystalline small molecule. As-cast BTR:PC$_{71}$BM devices were only able to achieve up to 4.9% PCE, however with the use of solvent vapour annealing efficiencies of over 9% were possible.[93] This was mainly due to a significant improvement in FF from 0.47 to 0.77, which the authors attributed to increased donor and acceptor domain sizes, affording greater interconnectivity through the active layer.

With the later development of NFAs, the efficiencies afforded from all-small molecule solar cells increased to 10-12%. Currently, a zinc porphyrin-based donor (ZnP-TBO), blended with the NFA 6TIC, can achieve the highest SM:SM solar cell PCE of 12.1%, also requiring a solvent vapour annealing step in order to afford a favourable nanoscale morphology.[94] It should be noted that the need for careful optimization of active layer treatments, such as thermal or solvent vapour annealing, is common in SM:SM solar cells. The use of such post deposition treatments have challenges to be scalable, limiting the industrial potential offered by SM:SM solar cells.

An effective method to further boost the PCE in organic solar cells is to add a third component in the bulk to form ternary organic solar cells. This approach has been widely used in fullerene- and NFA-based devices to: (i) increase the photon to current conversion upon adding a complementary absorbing donor and/or acceptor material, (ii) increase the V_{OC} by adding a higher LUMO acceptor or low HOMO donor, (iii) reduce charge recombination to maximize FF.[95] It is possible to achieve a variety of distinct BHJ morphologies in ternary blends, depending on the relative miscibility and aggregation of the three components. If we consider the addition of a third component, which can either be a second donor or acceptor material (D_2 or A_2), to an already established BHJ binary blend (D_1:A_1), there are a number of possible fates of the third component; it can can embed itself in the donor or the acceptor domains, co-crystallize with either the donor or the acceptor, or it can reside between the donor and acceptor phases. Depending on the position of the third component, the microstructure of either D_1 or A_1 can be tuned in the ternary BHJ through enhanced crystallization of one or both of the binary components, control of domain size, purity and the coherence length of the domains. This often results in improved charge carrier transport properties in ternary blends. It should be noted that the addition of a third component can also create an energy cascade, which favours charge separation, thereby reducing recombination in ternary blends. The ability to control recombination rates in ternary solar cells has allowed FFs approaching 80%. This originates from different processes such as charge or energy transfer as well as the formation of an alloy

between the donor-1:donor-2 (D1:D2) or acceptor-1:acceptor-2 (A1:A2). Adding a second acceptor (BTP-M) to a PM6:Y6 blend has recently led to ternary solar cells with efficiency of over 17%.[96] This arises from the formation of an molecular composite or „alloy" between the two NFAs; a single material, with properties, including FMO energy levels and crystallinity, that can be tuned by changing the ratio of the two components.[97] In PM6:Y6:BTP-M ternaries, the authors suggest that the „alloy" formed from the two NFAs simultaneously lowers the energy loss, by reducing the ΔE_{LUMO}, increases the quantum efficiency of the devices and enhances the hole and electron mobilities, via optimization of the blend morphology. Recently, it has been demostrated that adding O-IDTBR as a third component in PM6:Y6 reduces trap-assisted recombination and the ternary blend delivered a PCE of 16.6% and a FF of 0.76. In this ternary blend, O-IDTBR helps charge trasport due to its preferable mixing withing the Y6 phase resulitng in new mixed domains. Finally, the ternary blend showed enhanced photostability compared to PM6:Y6 binary due the deactivation of light-induced traps.[98] Enhancing the charge transport of PM6:Y6 has been also demonstrated by adding $PC_{71}BM$. In this ternary blend, the electron mobility increased, which leads to a more balanced charge transport, resulting in a FF of 0.77 and PCE of 16.5%.[99] The authors also found that $PC_{61}BM$ could reduce the size of Y6 aggregates, resulting in reduced non-radiative recombination losses. Not only have D:A1:A2 ternary blends based on PM6:Y6 been demonstrated, in fact, adding a D2 third component to the blend has been found to increase the charge extraction capabilities as well as decreasing charge recombination. In this ternary D1:D2:A, the authors added a third component small molecule donor (SM1) and the resulting ternary solar cells delivered a PCE of 16.55% with a FF of 0.77.[100]

3. The Thermodynamics of Phase Separation in Organic Semiconductor Blends

The initial picture of the ideal BHJ morphology was based on a two-phase morphology comprising pure donor and acceptor domains. However, since the observation of partial

miscibility in the benchmark P3HT:PC$_{61}$BM blend,[101] it is accepted that the presence of a third amorphous mixed phase is in fact beneficial, providing an energetic cascade between pure and mixed regions which enhances exciton dissociation.[41] However, the optimal morphology varies significantly depending on neat material and blend properties.

3.1. Material-Dependence of Optimal Bulk Heterojunction Morphology

In a binary blend, there are four D:A combinations that are possible in terms of material crystallinity: (semi-) crystalline/(semi-) crystalline, (semi-)crystalline/ amorphous (and vice versa) or amorphous/amorphous. The importance of crystalline domains has long been observed in OPVs. In fact, the most widely investigated binary blend incorporates P3HT as a semi-crystalline polymer donor and PC$_{61}$BM as a crystalline acceptor. Donor polymer crystallinity affects both the optical and electronic properties. It has been reported that increasing the crystallinity of P3HT, by increasing its regioregularity (RR), enhances absorption and charge transport.[102] Similarly, enhancing crystallinity by optimizing Mw has also been observed to improve device performance.[103,104] Nonetheless, it is necessary to control the degree of crystallinity for improved morphological stability, as demonstrated by the benefits of employing lower RR P3HT for suppressing excessive phase separation after annealing, attributed to the polymer's stronger tendency to crystallize.[105]

A similar correlation between crystallinity and performance has been observed in PffBT4T polymers, a family of low band gap polymers achieving higher efficiencies compared to P3HT. Upon increasing the side chain length in PffBT4T-2DT compared to PffBT4T-2OD, it was found that domain crystallinity and purity was reduced, leading to a reduction in device performance.[58] State-of-the-art polymers also include amorphous polymers, such as PTB7-based donors. Their inability to form pure ordered polymer domains leads to limitations in charge transport, and hence achievable active layer thickness.[58] However, polymers which are amorphous or display a low degree of crystallinity are important for achieving the required

microstructure when blended with many NFAs in order to suppress excessive phase separation.[75]

Optimising the extent of acceptor crystallinity is equally important for improving device performance. The presence of fullerene crystallites has been associated with (i) enhanced charge generation due to the presence of an energetic cascade between mixed amorphous domains and pure crystallites, as well as (ii) enhanced charge transport due to the improved charge mobility in crystalline domains.[106–108] Similarly, enhancing the crystallinity of non-fullerene acceptors has been associated with improved OPV performance in some systems, such as those involving ITIC or IDTBR acceptors.[71,109] However, the tendency of some acceptors to aggregate excessively induces undesirable large scale phase separation in OPV blends, as in the case of some PDI acceptors. In this case, various strategies are employed to suppress acceptor aggregation, including employing twisted PDI dimers or more complex 3D structures, leading to largely amorphous acceptors.[110,111] While many optimized polymer:small molecule solar cells have been shown to display a three-phase morphology (crystalline polymer domains, crystalline or amorphous acceptor aggregates and an amorphous polymer-rich matrix), blends relying on amorphous polymers can form a two-phase morphology at most. The composition of the amorphous mixed phases must also be optimized in order to strike a balance between improving charge generation, by increasing D:A interfacial area, while limiting bimolecular recombination.

Control of the degree of phase separation is also a common problem in all-polymer or all-small molecule solar cells.[112,113] In the former, large scale phase segregation is frequently observed due to the small entropic driving force for mixing between two macromolecules. This is demonstrated by the case of the NDI-based polymer acceptor P(NDI2OD-T2) in blends with P3HT as donor polymer,[114] as well as with BFS4 as a low bandgap donor polymer.[115] However, it is worth noting complete miscibility has been reported between the donor polymers FTAZ and PDPP3T in a fullerene-based ternary.[116] One method to control the degree of phase

separation is by tuning Mw; the case of PTB7-Th in combination with P(ThNDIThF4), another NDI-based polymer acceptor, displays increasing coarseness as acceptor Mw is increased.[117] This is expected based on the reduction in mixing entropy as molecular size increases. However, another example employing PTPD3T as donor and P(NDI2OD-T2) as acceptor showed little change in domain size as the Mw of either the donor or acceptor is increased, while the other is kept constant.[118] Furthermore, the opposite trend in domain size as a function of Mw has been reported for PPDT2FBT:P(NDI2OD-T2) blends (i.e. finer phase separation as Mw increases).[119] This was attributed to stronger donor aggregation at lower Mw, which drives stronger phase separation and/or more facile diffusion of the shorter chains (i.e. lower Mw). The above considerations highlight the diversity in 'optimal' morphology given the broad range of materials available with different properties. Apart from material properties, processing conditions play a crucial role in governing morphology formation.

3.2. From As-Cast to Optimized Morphology: Solidification Dynamics and Processing Strategies

Morphology formation during spin-coating, the most common method of active layer deposition in BHJ solar cells, is governed by both kinetic and thermodynamic factors. The former concerns variables such as drying rate and the kinetics of crystal nucleation and growth, while the latter includes solubility limits and the interactions between donor and acceptor molecules, which govern the liquid-liquid (L-L) two-phase region (i.e. the binodal or miscibility gap).[112]

The thin film active layer morphology formed on spin coating, is generally frozen far away from thermodynamic equilibrium given the fast-drying kinetics. The choice of solvent, solution concentration, and D:A ratio are the first parameters to optimize for achieving the best possible as-cast morphology. The choice of solvents allows to tune the morphology by varying solubility, viscosity and drying rate. Component concentrations near the solubility limit in a given solvent

induce earlier aggregation in solution, which freezes-in a smaller length-scale compared to lower concentrations.[120] The rate of solvent evaporation also affects the degree of phase separation, such that faster drying/ high volatility generally leads to shallower quench depths in the L-L two-phase region, i.e. finer structures. However, the effect of competing component crystallization on the phase separation length scale must also be taken into account, as highlighted by the observation of finer structures at slower drying rates in polymer: $PC_{61}BM$ blends. This was attributed to more effective $PC_{61}BM$ nucleation and growth during casting at slower rates, which reduced the fullerene concentration in the remaining liquid phase, thus leading to a shallower quench depth in the liquid miscibility gap.[121] Solution concentration also affects viscosity, which in turn determines how mobile molecules are in solution.

Another strategy to control the domain size involves the use of either additives or co-solvents. The former are more flexible in terms of solvent choice, and are used in comparatively smaller concentrations to the latter, but have the same purpose.[112] They are used to either reduce the extent of phase separation,[122,123] or to promote it and/or induce a higher degree of crystallinity.[124,125] In the widely investigated P3HT: $PC_{61}BM$ system, the use of additives was found to increase transistor hole mobility by increasing the degree of order in P3HT.[126,127] Briefly explained, additives or co-solvent can act as a good or bad solvent for one of the blend components, thus allowing to control the onset and extent of S-L and/or L-L demixing. Detailed understanding of additive choice and its effect on solidification dynamics are beyond the scope here, and are reviewed elsewhere.[112] The choice of D:A ratio also influences the extent of phase separation. In various polymer/fullerene blends, it has been observed that increasing acceptor content beyond a threshold value induces the formation of pure acceptor domains, alongside the mixed matrix. Such domains are favourable for improved electron percolation and mobility, as well as for enhancing charge separation.[39,107,128] The latter effect has also been recently reported for a blend incorporating EH-IDTBR as non-fullerene acceptor.[129] Finally, another parameter that is used to optimize morphology during deposition is the processing

temperature. However, this is mostly relevant to polymers (such as the PffBT4T family of polymers), which display temperature-dependent aggregation behaviour.[58,130] Control of solution and substrate temperatures is a key requirement for controlling polymer aggregation in order to achieve optimal microstructures in these blends, such that high polymer crystallinity is coupled with reasonable domain size.[58]

In some cases, tuning of deposition parameters is sufficient for optimizing BHJ morphology.[131] However, additional post-processing treatments are often required. These include either thermal (TA) or solvent vapour annealing (SVA). In some cases, TA is only used to ensure complete solvent removal. Otherwise, the effect of both techniques is to allow microstructure rearrangement by facilitating molecular mobility in the polymer matrix. With TA, this is done by heating the as-cast film near the glass transition (T_g), while SVA is based on allowing the vapour of a chosen solvent to penetrate the film, thus partially dissolving it to enable molecular diffusion.[112,132] An example is the widely investigated P3HT: $PC_{61}BM$ blend, where thermal annealing of the active layer was observed to be crucial for increasing the degree of crystallinity of P3HT, thus improving charge transport.[52,128] A similar effect occurs in acceptor domains in blends of P3HT with O-IDTBR as an NFA,[71] as well as in other material combinations, including SM:SM and polymer:polymer binaries.[133,134]

Most of the understanding of the techniques and mechanisms of BHJ morphology optimization are based in large part on P3HT: $PC_{61}BM$, as well as on other polymer:fullerene blends. However, there is currently a wide range of both polymers and acceptors available, prompted by the need for improved light harvesting, energy level tuning, cost-efficiency, and stability (amongst other requirements), compared to more traditional blend types. Considering the intricacy of morphology formation from solution and subsequent post-processing, in addition to the possibility of employing either SM:SM or polymer:polymer binaries in addition to polymer:SM blends, it is thus clear that the understanding established for polymer:fullerene blends cannot always be directly applied to more novel blends. For example, as highlighted

above, opposing dependencies of microstructure on Mw have been reported for polymer:polymer blends. Furthermore, the recent observation of strong differences in the Mw dependence of device performance in P3HT:NFA blends based on IDTBR acceptors led the authors to suggest the need to investigate the effects of Mw on a case-by-case basis.[72] Such an approach is far from ideal given the interest and importance of bringing OPV technology closer to commercial viability. As such, increasing efforts are dedicated towards developing rational and quantitative approaches to BHJ engineering.

3.3. Towards Rational and Predictive Blend Selection and Optimization

Thus far in the field of OPVs, morphology optimization has been based on a time-consuming and costly trial-and-error approach, where a detailed understanding of the characteristics of morphology is only obtained post-fabrication. In order to circumvent these limitations, there is a need for faster rational and/or quantitative models and techniques to guide rapid material design and selection, as well as reduce the amount of device optimization required.[135-137]
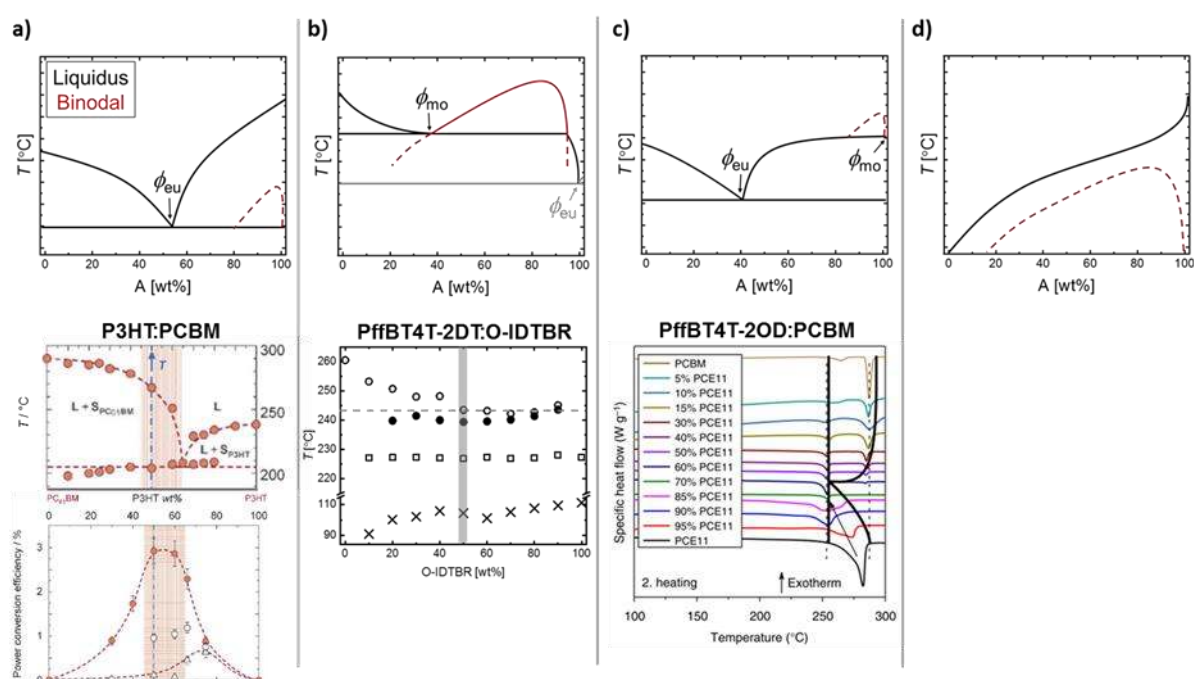

Figure 4. (a-d; top panels) Schematic models of various types of phase behavior in polymer:small molecule acceptor binaries ('A' denotes the small molecule concentration). Black and grey curves denote liquidus lines determined from DSC; black and grey horizontal lines denote eutectic or monotectic reactions. Red curves indicate the binodal. (a-d; bottom panels) Corresponding examples from literature. (a; top) Eutectic T-ϕ diagram with a

submerged miscibility gap, which suggests strong D/A interactions; (a; bottom) P3HT:PCBM T-ϕ diagram and OPV device performance as a function of composition. Adapted with permission.[108] Copyright 2008, Wiley-VCH Verlag GmbH & Co. KGaA. (b; top) Monotectic T-ϕ diagram; the presence of a eutectic reaction (highlighted in grey) depends on whether or not the acceptor is crystalline; (b; bottom) T-ϕ diagram of PffBT4T-2DT:O-IDTBR, suggesting monotectic behavior. Reproduced with permission.[142] Copyright 2020, Wiley-VCH Verlag GmbH & Co. KGaA. (c; top) Eutectic T-ϕ diagram with a monotectic composition near the pure acceptor axis due to a high acceptor melting temperature and weak D/A interactions. The constructed T-ϕ diagram from DSC of PffBT4T-2OD:PCBM (c; bottom) evokes such a system.[46] Provided under a Creative Commons CC BY license. (d; top) Example of a T-ϕ diagram in an amorphous polymer:crystalline small molecule binary with strong D/A interactions. An example of such a system is PCDTBT:PCBM.[38]

As discussed above, phase separation length scale, domain purity, degree of crystallinity and domain interconnectivity are very important parameters for achieving an optimal BHJ microstructure. Early efforts to rationalize device optimization include the simple model suggested for optimizing D:A ratios, based on eutectic temperature-composition (T-ϕ) diagrams constructed from differential scanning calorimetry (DSC) (**Figure 4A**).[108] The authors suggested that the highest performance is related to the occurrence of acceptor crystallites which ensure effective electron percolation.[108,138] Such behaviour was suggested to require hyper-eutectic compositions (with respect to acceptor wt%). Eutectic phase behaviour has since been reported for many OPV blends comprising P3HT with either fullerene or nonfullerene acceptors,[72,138] as well as in blends based on other donor polymers.[107,139–141] While simple and based on an easily accessible technique, this model is limited to crystalline/crystalline polymer/small molecule blends which display eutectic behaviour. Furthermore, its applicability to blends incorporating high-performance low bandgap polymers lags behind. Recently, the model was extended to discuss the relationship between phase behaviour and optimal D:A ratio in monotectic blends incorporating PffBT4T-2DT as a low bandgap donor and O-IDTBR or O-IDFBR as NFA (**Figure 4B**).[142] Such blends are characterized by low liquid-miscibility. Optimal composition was rationalized in terms of the interplay between S-L and L-L demixing for a controlled phase separation length scale. This extended the discussion of the relationship

between phase behaviour, ratio optimization and performance to the case of an amorphous acceptor, namely O-IDFBR, but additional work is needed to demonstrate its applicability to blends of similar crystalline polymers with other acceptors.

Various types of T-ϕ diagrams are schematically illustrated in Figure 4, with corresponding experimental examples from literature. **Figure 4C** illustrates the case where the high melting temperature of the acceptor leads to a monotectic composition that is pushed towards the pure acceptor axis and a eutectic point which occurs at intermediate composition,[46,143] which may be the type of behaviour displayed by PffBT4T-2OD:PC$_{71}$BM based on the T-ϕ diagram visualized from the reported DSC data (Figure 4C). Another case is that of an amorphous polymer with a crystalline acceptor, such as PCDTBT:PC$_{71}$BM (**Figure 4D**). [38,45,144]

It is important to note that the binodal curves illustrated schematically in Figure 4 are a guess and, as discussed further below, their measurement is not simple. However, the effect of the binodal on the shape of the liquidus highlights the importance of measuring T-ϕ diagrams for a more accessible but qualitative evaluation of component interactions, and for further exploring the potential of ratio optimization based on phase behaviour understanding.

Despite the fact that the phase behaviour/performance model remains limited in scope and requires further work to verify its applicability to a wider range of materials, thermal analysis is an easily accessible tool and provides a wealth of information on bulk microstructure and morphological stability. In fact, the potential of several thermal analysis techniques to play a more significant role in OPV active layer design and optimization has only recently gained interest. A recent report explores the potential of DSC as a tool for a more predictive understanding of the relationship between component crystallinity, relative degree of phase separation, device performance and stability in a given blend.[145] The suggested model is based on the commonly observed shift in non-fullerene acceptor cold-crystallization temperature (T_{cc}) upon blending with a polymer donor.[45,146] The strength of the T_{cc} depression, dictated by the

polymer's degree of crystallinity, was suggested to correlate with domain size and purity, as well as morphological stability.[145]

Furthermore, ongoing efforts explore the potential of using T_g as a promising method to quantify absolute composition in the mixed amorphous phase.[147] This method relies on fast scanning calorimetry; in contrast to DSC, very little material is required such that investigation can be performed directly on spin-cast thin films, prepared in the same way device active layers are processed.[147] The larger sample size required for DSC means that spin-casting cannot be used as films are not thick enough, so samples are instead drop-cast.

The interest in quantifying the composition of amorphous domains can be traced back to the first observation of partial miscibility in OPV blends in P3HT: $PC_{61}BM$.[148] The degree of mixing in these domains is dictated by the interactions between donor and acceptor molecules, which govern the L-L miscibility gap. A common approach to evaluate these interactions has been the use of the Flory-Huggins (FH) interaction parameter (χ_{FH}) estimated using the melting point depression method,[137,149–154] although other methods and approximations have been used.[46,155] However, until recently,[38] most of these analyses have been narrow in scope and/or unclear in the true meaning of the extracted interaction parameter, similar to what happened in the field of polymer blends decades ago.[156] In its original formulation, χ_{FH} is a measure of the amorphous/amorphous (a/a) miscibility in a polymer solution of a semi-crystalline polymer mixed with an amorphous solvent.[156] It quantifies the degree to which the amorphous diluent is mixed in amorphous polymer domains; this is dictated by the molecular interactions between polymer and diluent, which in turn are governed by the chemical structures of both components. However, direct extraction of χ_{FH} (i.e. amorphous/amorphous miscibility) from melting point depression data is only valid for certain crystalline/amorphous blend types. In contrast, in other blend types, melting point depression data must first be corrected for the effect of crystalline/amorphous interactions in order to accurately estimate a/a miscibility.[38,144,156,157] Additionally, the melting point depression method evaluates the interactions near the melting

point,[154] which is much higher than device processing temperatures. Recently, two methods have been reported as a more quantitative approach to the evaluation of the temperature dependence of χ_{FH}, i.e. χ_{FH} (T).[38] The first method uses secondary ion mass spectrometry (SIMS) to measure the degree of inter-diffusion between polymer and acceptor films stacked in a bilayer configuration as a function of annealing temperature. The temperature-composition (T-ϕ) data points thus obtained are then fitted with the FH equation for the binodal, allowing χ_{FH} (T) to be determined. The second method uses scanning transmission X-ray microscopy (STXM) to measure an effective (uncorrected) interaction parameter after aggressive thermal annealing to induce maximal demixing; this provides a measure of the maximum possible purity of the polymer-rich amorphous phase, in the presence of acceptor crystals. To obtain χ_{FH} (T), the value from STXM is corrected with the crystalline/amorphous interaction parameter ($\chi_{c/a}$), determined from DSC.[38] These methods are easiest to apply to blends incorporating an amorphous polymer and acceptor. Crystalline polymers incur an added complexity in that their degree of crystallinity must be taken into account.[144] While both methods constitute a significant advance in quantifying χ_{FH} and its effect on performance in OPV blends, the techniques involved are not easily accessible. A recent report suggests a more accessible method for evaluating the uncorrected interaction parameter using UV-vis absorption spectroscopy and visible light microscopy.[136]

3.4. Bulk Heterojunction Thermal-Stability Considerations

Understanding the mixing thermodynamics and the kinetics of film formation is not only crucial for achieving an optimal BHJ microstructure, but also for ensuring its stability, a key parameter for commercial applications. Since the active layer morphology is generally frozen far away from thermodynamic equilibrium, given the fast drying kinetics, degradation of the optimized morphology may occur, leading to device deterioration. There are two possible morphology degradation pathways, namely demixing in the amorphous domain or crystallization.[45] Active

layer thermal stability is governed by a combination of thermodynamic and kinetic factors, including (i) how far the composition of the amorphous phase (if any) is from thermodynamic equilibrium, (ii) the tendency of a given component to crystallize, (iii) T_g and (iv) molecular diffusion.[45,158]

Morphological instability is a common problem for the widely investigated P3HT:PC$_{61}$BM system, where optimization of the as-cast morphology requires thermal annealing above the blend T_g. This enhances the crystallinity of P3HT, leading to improved performance. However, this also generally leads to the formation of micrometer-size fullerene crystals which degrade performance. Several strategies have been developed to suppress excessive fullerene crystallization, including the use of amorphous fullerene alternatives,[158,159] or by tuning polymer properties (such as RR or side chain length).[105,160] Another strategy is employing polymers or fullerene acceptors which induce a higher blend T_g.[161,162]

Recent efforts focus on understanding the factors that govern morphological stability in NFA-containing blends. Similar to fullerene-based blends, T_g and diffusion coefficients evidently remain crucial parameters for the suppression of amorphous demixing and/or crystallization-induced phase separation.[45] However, there are also significant differences between fullerene and NFA-based devices given the difference in chemical structure and size; for instance, superior thermal stability in blends incorporating EH-IDTBR as NFA has been attributed to a smaller diffusion activation energy.[45] Furthermore, it has been found that in PBDB-T:ITIC blends, the acceptor undergoes crystallization via two different processes above and below its T_g.[158] The unique diffusion-limited crystallization below T_g leads to high thermal stability, while crystallization-induced degradation occurs above T_g, similar to fullerene-based blends. While similar morphology degradation can be observed in SM:SM binaries, domain composition and size in all-polymer solar cells are more robust towards thermal degradation given the lower molecular mobility and chain entanglements.[163]

As highlighted in the previous section, morphological stability is a crucial parameter to take into account in the search of a more rational and comprehensive approach to BHJ engineering. The challenge imposed by such a target is evident by considering the fact that optimal microstructure and morphological stability vary significantly depending on material properties. Furthermore, in line with increasing efforts to bring OPV technology closer to commercial viability, it is important to note that spin-coating is not compatible with large-scale production. Viable deposition techniques (e.g. inkjet printing) involve different dynamics during film formation. Thus, while it is crucial to have general guidelines for BHJ design and optimization for lab-scale devices processed by spin-coating, OPV commercialization is also dependent on achieving a similar level of understanding for deposition techniques compatible with large scale production. Such investigations currently lag behind, but should increasingly become a key point of focus for future research.

4. The Influence of Bulk Heterojunctions on Charge Transfer States

As discussed above, the nature, and eventual fate, of the CT states dictate whether exciton scission or recombination occur; this will directly influence the performance of the OPV device. Therefore, an understanding of how the CT states differ in a range of blends, and the subsequent effect on factors such as recombination, voltage losses, the mobility and lifetime of charge carriers, can afford guidance on designing OPV blends capable of ever-greater PCEs.

4.1. CT State and Non-Radiative Voltage Losses

Thermodynamics requires that at open circuit, an ideal solar cell features a radiative quantum efficiency of unity, defining the reciprocity that a good solar cell is intrinsically a good LED.[164] Internal luminescence yields of close to 100% have been observed for both GaAs and perovskites.[165,166] In contrast, organic semiconductor devices display either a high efficiency conversion from radiation energy into electricity in bulk-heterojunction solar cells or high

electroluminescence yields in OLEDs.[167,168] The low external quantum efficiency of electroluminescence(EQE$_{EL}$) of donor and acceptor BHJ solar cells is assigned to the large non-radiative CT state decay, primarily responsible for the open circuit voltage losses of these devices.[15,169-175] A complete evaluation of the open circuit voltage losses in OPV considers both radiative and non-radiative recombination losses as well as the conversion of excitons in the pristine BHJ components into delocalized CT states. Efficient conversion from the CT state to free charges can be related to a minimum Gibbs free energy offset between the CT and the local excitation (LE) (ΔG_{LE-CT}) of D or A, which has been empirically calculated to be around 0.3 eV.[176-178] This scenario affords non-radiative pathways, resulting in a reduced V$_{OC}$. Non-radiative voltage losses are defined according to Equation 1, where k$_B$ is Boltzmann's constant and T is the cell's operational temperature.

$$(\Delta V_{OC,nr} = -k_B T/q \cdot ln(\text{EQE}_{\text{EL}})) \tag{1}$$

Typically, fullerene-based OPVs deliver an EQE$_{EL}$ of 10^{-6}, which corresponds to $\Delta V_{OC,nr}$ of 350-400 mV.[179] As recently reported in the case of fullerene-based solar cells, a certain threshold of driving energy was found to be necessary for high charge generation, below which the devices usually suffer from low internal quantum efficiencies (IQE). Moreover, the same group recently reported a large set of D-fullerene material systems based on BHJ and bilayer architectures. With an energy difference between the ground and CT states ranging from 0.7 eV to 1.7 eV, it was found that $\Delta V_{OC,nr}$ increases by decreasing the energy of CT state (E$_{CT}$).[175] This correlation arises from an increased wavefunction overlap between relaxed CT states and higher order vibrational modes of the ground states which promotes non-radiative pathways. Interestingly, the authors found that by analyzing the low-energy tail of the EL spectra, the non-radiative decays occur via D-C$_{60}$ CT states rather than C-H vibrations. Therefore, non-radiative recombination losses are an intrinsic loss mechanism in fullerene-based solar cells. The recent development of NFAs, however, proved that high photocurrent generation despite a very small energy offset (<0.3 eV) is possible. External quantum efficiency close to unity for materials

with an E_g of 1.5 eV as well as FF above 80% have been reported. Solving CT related V_{OC} losses is one of the ultimate fundamental challenges and would allow OPV devices to achieve parity with the most efficient photovoltaic technologies. This will require solving the limited reciprocity in OPV devices.

To date, few NFA-based systems with ELQY > 10-2 % have been reported. Still, a fundamental explanation that would allow to consistently design high efficiency OPV semiconductors is missing. Whilst significant improvements in maximing J_{SC} and FF have been made through material design and engineering device strategies, overcoming V_{OC} losses remains an open challenge in the pursuit of PCEs of over 20%. It has been proposed that long-lived charge carriers on the donor matrix particularly in polymer:PDI systems leads to high EQEEL.[14,179] In particular, a delayed photoluminescence has been observed on the microsecond time scale, longer than the pristine materials. The authors demonstrated that this long-lived PL arises from radiative nongeminate recombination of charges occurring via CT states located near the energy of the polymer singlet state. Recent reports suggest that low energetic offsets between D and A result in the hybridization of CT states with the lowest emissive LE of the two components. This leads to suppression of nonradiative voltage loss to values as low as 0.23 V which is concomitant with an increased CT state luminescence and the overlap of the EL of the blend with the EL of the NFA. The small ΔE_{LE-CT} values in NFA based systems due to hybridization between the CT and LE states questioned the use of the two-state Mulliken–Hush approach for these systems.[180,181] In this approach, non radiative recombination losses are described by Marcus' theory: the CT absorption is described as the transition from GS to CT featured by a Gaussian shape and the electronic coupling between the GS and CT is related to the adiabatic transition dipole moment. However, the two-state model does not take into account the high-frequency intramolecular vibrational modes that contribute to the electron–vibration couplings. For this reason, a three-state model has been recently developed, including a quantum-mechanical treatment of the vibrational modes. This has a significant effect on the shape of the

absorption band of the D-A complex, especially for cases with ΔE_{LE-CT} lower than 1eV. Moreover, in the case when no low-energy CT states are not detected with the common techniques such as photothermal deflection spectroscopy (PDS) and Fourier transform photocurrent spectroscopy (FTPS), the use of a three-state.[182,183] Similarly, introducing the effect of the wave function overlap between singlet and CT state, explained by the oscillator strength of the CT to GS transition, $\Delta V_{OC,non\ rad}$ has been predicted to approach values as low as 0.17V.[184] It is then not surprising that with these design rules, novel organic semiconductors materials with an almost zero energy offset between the D and A materials for maximizing V_{OC} have been developed. Between those blends, the discovery of PM6:Y6 boosted the performances of OPV devices with values over 17%.

4.2. PM6:Y6 Based Solar Cells

Y6-based organic solar cells exhibit amongst the highest power conversion efficiencies to date, and at present are attracting significant research interest with respect to material optimization and fundamental understanding, particularly focusing on the photophysics and blend morphology. Several reports suggest that this blend feature a very high internal quantum efficiency (IQE) in excess of 95%, which suggests an efficient charge generation and extraction.[185] In fact, a detailed study on these processes using time-delayed collection filed and IQE measurements showed negligible losses due to exciton and geminate recombination in a PM6:Y6 blend, the reason of the high FF and J_{SC} in the blend. Contrary to previously reported NFA-based systems, PM6:Y6, together with high FF and J_{SC}, shows an exceptionally high V_{OC}. This arises from a negligible difference between S1 and ECT (0.05 eV), and a total voltage loss considering both radiative and nonradiative recombination of 0.49 eV, amongst the lowest reported to date (**Figure 5a-c**). Temperature-dependent J-V measurements, in fact, reveal nearly barrierless free-charge formation and efficient charge generation as low as 100 K. Computational studies on PM6:Y6 show that the A-D-A-D-A molecular architecture of Y6

induces a large quadrupolar moment on a molecular scale, and its dimerization in a unit cell create an electrostatic bias potential able to compensate the coulombic interaction of the CT, therefore enabling barrier-free CT state dissociation (**Figure 5d-e**). [185] Moreover, the calculation of the Urbach energy extracted from FTPS measurements, revealed an E_U (26.7 meV) near the thermal energy (kT), indicating low energetic disorder in the system. Charge recombination processes are often associated with the blend microstructure, which is generally investigated by GIWAXS measurements. However, while this technique has been widely adopted for fullerene-based systems, NFA-based blends feature very similar 2D patterns which makes it challenging to differentiate the D and A contribution. In this respect, PM6:Y6 blends have been characterized by solid-state ^{19}F magic angle NMR spectroscopy, to provide information about the intermolecular and intramolecular interaction of the donor and acceptor materials. The results indicate that Y6 molecules in the blend are characterized by a signal with a narrow distribution, whereas in the neat Y6, two different packing motifs were resolved with the one dimensional ^{19}F ssNMR.[82] This indicates a more uniform packing of the Y6 molecules in the blend, whereas, the one dimensional ^{19}F ssNMR results indicate that the PM6 packing remains unaffected upon addition of Y6, confirming that the ordering of the PM6 observed in the neat film is also retained in the blend. This sub-nm scale phase segregation between PM6 and Y6 explains the low charge recombination in the blend as well as the superior charge extraction capability, confirmed by the relatively small bimolecular recombination coefficient k_{bm} of 2-6 x 10^{-13} cm^3 s^{-1}. The low k_{bm} value should allow the fabrication of thicker devices, since similar values have been achieved with P3HT:PCBM and P3HT:O-IDTBR blends, which delivered high PCE with active layer thickness of over 300 nm.[186]
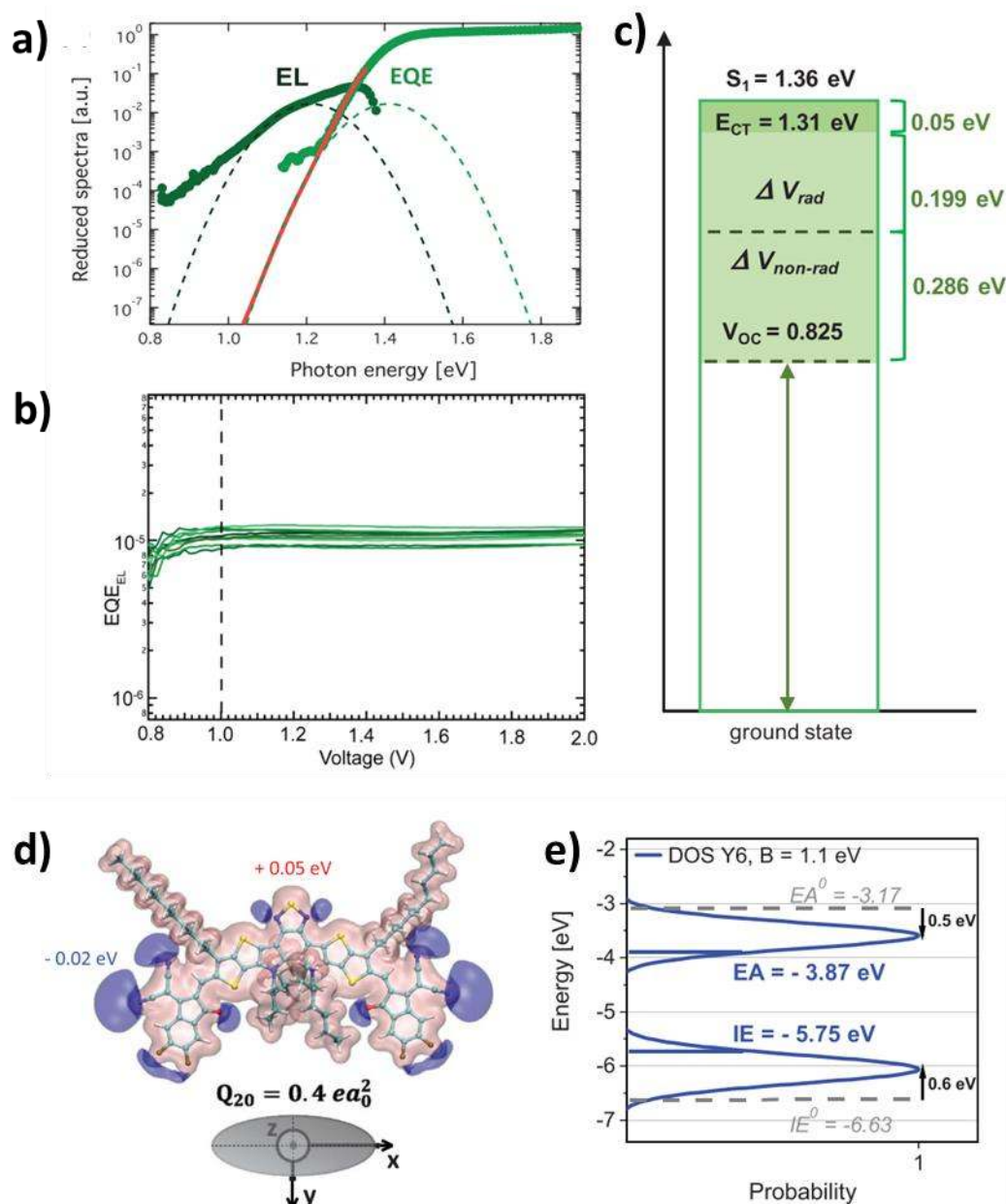
Figure 5. (a) EQE and EL spectra of PM6:Y6 blends; (b) Measured EQE_EL versus applied bias for PM6:Y6 solar cells; (c) Schematic representation of radiative and non-radiative voltage losses. (d) Isosurfaces of the electrostatic potential and (e) calculated density of states (DOS) for electrons (EA) and holes (IE) in a model crystal of Y6. a-c reproduced with permission.[82] 2017, WILEY-VCH Verlag GmbH & Co. KGaA, Weinheim, and d-e reproduced,[185] provided under a Creative Commons CC BY license.

4.3. Charge Carrier Mobility and Recombination

In general, the FF is defined as the competition between the charge generation and extraction.[187] Several processes, such as trap assisted recombination, bimolecular recombination, and parameters such as charge carrier mobility and lifetime play a role in

maximizing the FF.[188–194] Trap assisted recombination, is an inherent recombination in OPV

blends, arising from the energetic disorder of organic materials.[195–197] Bimolecular

recombination rates of holes and electrons, on the other hand, are usually referred to as

Langevin recombination.[198] The Langevin recombination coefficient β_L is given by Equation

2, where μ_h and μ_e are the effective charge carrier mobility of holes and electrons, respectively,

ε_0 is the vacuum and ε the relative permittivity.

$$(\beta_L = \frac{q(\mu_h + \mu_e)}{\varepsilon \, \varepsilon_0})$$ (2)

In this representation, hole and electron need to recombine instantaneously, otherwise the model

fails to describe the recombination rates correctly. In this case, this is described as reduced, or

non-Langevin recombination. Comparing the measured bimolecular recombination (β) with the

calculated Langevin pre-factor underpins the recombination mechanism, where $\beta/\beta_L < 1$

indicates reduced Langevin recombination.

Several approaches have been used in both fullerene and non-fullerene-based devices to reduce

these recombination processes. For example, post deposition methods such solvent and thermal

annealing have been adopted to modify the microstructure of as-cast blends in order to achieve

favorable morphologies for efficient charge extraction.[199–202] In fullerene-based solar cells, an

effective method to remove trap states is the solvent treatment of the bulk surface. A post

deposition methanol treatment of PTB7:PC$_{71}$BM devices resulted in the enhancement of all

photovoltaic parameters, due to an increased built-in voltage across the device arising from

passivation of surface traps and a corresponding increase of surface charge density.[203] For

several fullerene-based blends the addition of high boiling point solvents, such as 1,8-

diiodoctane (DIO), to the solution was an effective method to enhance the aggregation of the

donor and at the same time reduce the fullerene derivative domain size, due to their poor

solubility in the solvent and high solubility in the additives, respectively.[204,205] However, as

recently demonstrated, this cannot be easily translated to a nonfullerene based blend. In fact, in

PTB7-Th:ITIC, the addition of 3% by volume of DIO results in a more coarse morphology compared to the pristine blend, which increases charge recombination.[206] This is opposite to the trend in PTB7-Th:PC$_{71}$BM devices.

The PCE of OPV devices is rapidly increasing to values in excess of 18%, which makes this technology potentially suitable for upscaling to real world applications. However, roll-to-roll and spray coating, the common deposition methods in industry, require relatively thick blends to be processed without pin-holes. For this reason, P3HT-based devices have been adopted in combination with both fullerene and nonfullerene acceptors. In fact, both P3HT:PC$_{61}$BM and P3HT:O-IDTBR feature the lowest β values in the range of 10^{-13} cm^3 s^{-1} and 10^{-14} cm^3 s^{-1}, respectively.[186] This low bimolecular recombination allowed the fabrication of OPV devices with thicknesses of over 300 nm without a drop in PCE (**Figure 6a-b**). Instead the majority of D:A BHJ OPV feature β values in the range of 10^{-10} - 10^{12} cm^3 s^{-1} and the corresponding devices are generally limited to active layer thicknesses of 100-120 nm.[207] Different approaches have been used to increase the thickness of OPV devices. It has been found that an inverted off-center spinning method increased all PV parameters in PTB7-Th:PC$_{71}$BM by creating a more favorable vertical D:A composition gradient which improves charge extraction with active layers of over 200 nm.[208] Additionally, adding a third component in the blend with superior charge transport properties has been found as a viable method to decrease charge recombination and allow, at the same time, the fabrication of thick devices.[95,99,146,209–211] This is the case of the ternary solar cell based on PTB7:Si-PCPDTBT:PC$_{71}$BM which features high FF with a relatively high thickness.[212] At the same time, the formation of an alloy between two NFAs has facilitated ternary solar cells with PCE of over 14% together with 300 nm thick active layers due to the strong aggregation of the two acceptors, allowing an efficient charge transport in the thick blend.[213]
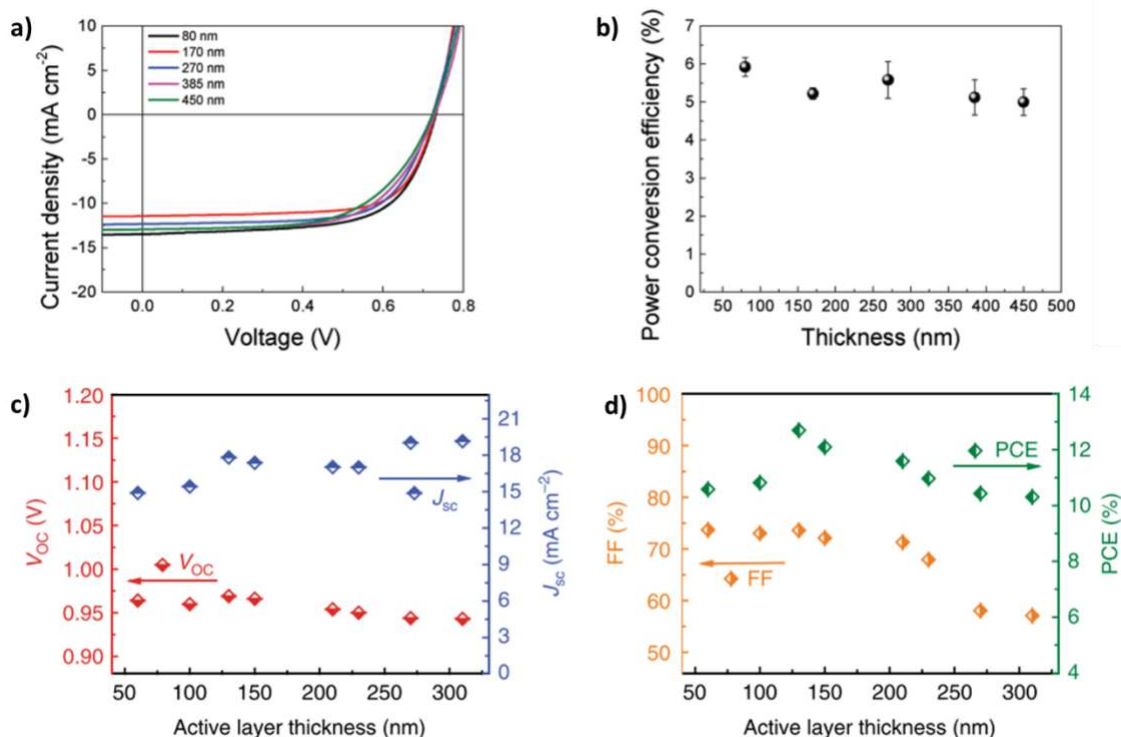
Figure 6. Current-voltage characteristics (a) and corresponding PCE (b) as a function of thickness for P3HT:O-IDTBR solar cells. Voc - Jsc (c) and FF – PCE (d) values as a function of thickness for PTQ10:IDIC solar cells. a-b reproduced with permission.[186] Copyright 2017, WILEY-VCH Verlag GmbH & Co. KGaA, Weinheim, b-c reproduced,[214] provided under a Creative Commons CC BY license.

Recently, a novel polymer donor (PTQ10) has attracted a lot of attention in the OPV community due to its low synthetic cost and the high performance (over 16%) in combination with low bandgap NFA.[214,215] Despite the high efficiency, the synthesis of PTQ10 is a 2-steps reaction from cheap raw materials, with the overall yield in the excess of 87%. In addition, devices based on PTQ10:IDIC, exhibit a PCE of over 10% with active layers of 300 nm, due to the relative high mobility of the materials (**Figure 6c-d**). The combination of these unique properties makes PTQ10-based devices a great candidate for the translation of OPV from lab-to-fab.

5. The Bulk Heterojunction in Organic Photodetectors

As previously discussed, the employment and understanding of organic semiconductor thin film bulk heterojunctions, has been predominantly driven by the development of OPV applications. Organic photodetector (OPD) technologies, based on organic photodiodes, have, to date, not

yet gained the same level of scientific attention.[216–222] Similar to the photophysical processes of OPVs, the control of the BHJ morphology and excitonic nature of organic materials is key to the development of successful OPD devices. The blending of donor and acceptor materials in a BHJ architecture is widely used in OPD to enhance exciton dissociation at the D:A interface and therefore improve charge extraction via the bicontinuous percolating network. In contrast to OPV, which operates under forward bias for light to power conversion, OPD devices operate under reverse bias for light detection. Moreover, in OPV the PCE is the common figure of merit used to compare the performances of devices, in OPD devices, it is necessary to simultaneously optimise Specific Detectivity (D*), EQE, Responsivity (R), dark current (J_d), cut-off frequency, transient time and noise equivalent power (NEP), which can be challenging.[223,224] In particular, a low J_d, defined as any current generated under an applied reverse voltage in the absence of light, allows the conversion of low levels of light into a detectable electrical signal, without the need of applying a significant external negative voltage.[225,226] High J_d values are often attributed to charge injection from the contacts into the semiconductor, or thermally generated charges in the bulk.[227] These limitations can be overcome by adopting a planar heterojunction (bilayer) made via sequential vacuum deposition of individual D and A materials. This structure allows the formation of pure D (or A) phases at the respective electrode, which can effectively block charge injection under reverse bias. However, low photocurrent is often observed for this configuration, which limits the R of photodetectors, for example. A promising approach to form relatively pure D and A, close to the device contacts, whilst simultaneously achieving partial D:A interpenetration in the bulk is the sequential solution deposition of the D and A materials.[228] In this method, the two components are sequentially deposited from solution, resulting in a well-mixed inter-diffusion phase in the bulk, whilst pure domains at the contacts can limit charge injection from the electrodes. The active layer thickness in OPDs is also known to influence device performance; J_d is known to decrease with increasing active layer thickness. This has been attributed to a decrease in extrinsic defects,

such as film inhomogeneity and pinholes, and the reduction of image charge effect, leading to a higher effective barrier for charge injection. Alternative approaches to minimize the dark current of OPDs, whilst maintaining the BHJ architecture to maximize the photocurrents, have been proposed. For example, donors with deep HOMOs (or acceptors with shallow LUMO) would minimize charge injection. Another common strategy consists of improving charge selectivity at the contacts by using hole (and electron)-blocking (HBL and EBL respectively) contacts.[229] HBL and EBL contacts maintain an energy cascade between the BHJ and the electrodes, but raise the energetic barriers for charge injection, resulting in reduced dark current in OPDs. Currently, the lowest J_d values range between 10_{-6}-10_{-7} mA cm$_{-2}$ and the corresponding OPD devices deliver a linear dynamic range over several orders of magnitude of light levels and low NEP values. While maintaining the processability of OPV blends, the BHJ of an OPD device can be tuned from both a chemical design and device engineering perspective, in order to tune the detection window across the UV-VIS-NIR region of the electromagnetic spectrum. Before the advent of NFAs, OPD devices based on donor:fullerene blends were limited by low R in the visible region in comparison to silicon detectors. Therefore, OPD technologies were mainly useful for indirect-conversion of X-rays. This was demonstrated by fabricating BHJ OPD containing PbS nanocrystalline quantum dots added to P3HT:PCBM blends.[230] These hybrid OPDs demonstrated a detection up to 1.8 µm, a J_d of 2.5x10$_{-2}$ mA cm$_{-2}$ at -5 V, EQE of 51% and fast temporal response of less than 100 µs. The authors demonstrated NIR imaging by integrating the OPD on amorphous silicon active matrix backplanes. These imagers were able to achieve both snapshot as well as video recording, at a frame rate of 5 Hz, of two woodlice illuminated at 1310 nm.

The negative voltage applied to imagers integrated with OPDs is necessary for (i) keeping the diodes sufficiently charged, which implies that the readout charge is proportional to the amount of extracted charges; (ii) increasing the response speed of the diode and therefore allowing

video recording.[231] The slow dynamics of OPDs is one of the main limitations of this technology compared to their inorganic counterparts, with device speeds that are several orders of magnitude lower than seen in silicon photodiodes. This is attributed to the lower charge carrier mobility of organic semiconductors, which limits charge extraction and therefore the thickness of OPDs in the range of 100-1000 nm. Generally, thick BHJ active layers are beneficial for lowering J_d; a result of reduction in pinholes and film defects. It has been demonstrated that it is possible to enhance the speed of OPDs by the deposition method of the BHJ or by using high boiling point solvent additives. For example, spray coating BHJ of fullerene and nonfullerene-based OPDs result in increased charge carrier transient time as well as cut-off frequency.[6] This has been attributed to the simultaneous effects of improved photon absorption and reduced pinholes and defects, afforded by thicker active layers. Another approach is the introduction of DIO, which resulted in enhanced device speed from 738 Hz to 64 kHz.[232] As discussed previously, DIO has often been employed in OPVs in order to control phase separation and crystallinity in BHJs. Similarly, it has been used in OPDs to reduce the size of domains in a BHJ and improve the polymer crystallinity, resulting in greater charge carrier mobilities and reduced charge recombination.

An exciting application for OPDs is in pulse oximeters, a non-invasive medical sensor for heartbeat monitoring and blood oxygenation, exploiting light absorption variations between oxygenated and deoxygenated blood in the visible and near-infrared spectrum. Recently, an ultraflexible oximeter based on highly efficient green and red polymer light-emitting diodes (LEDs) and P3HT:PCBM as active layer of the OPD has been demonstrated.[233] The device was laminated to the skin using adhesive tape. The V_{oc} of the OPD was monitored to measure the absorption of incident green and red light by the blood and consequentially delivering the corresponding pulsating photoplethysmogram signal. Since many of the reported oximeters use a single photodetector, with two different coloured LEDs, the OPD cannot distinguish the

wavelength of the incident light. Thus, the two LEDs must operate in a sequence, at a given frequency, and the OPD is synced to this using optoelectronics driving hardware and software. These additional requirements can result in bulky form factors and increased device power consumption, which can be an issue for the commercial application of these devices. More recently, an ambient light oximeter (ALO), which works without the need for LEDs, was reported.[234] Two OPDs were utilized; the first a PCDTBT:PC$_{71}$BM BHJ blend, and the second a P3HT:O-IDTBR BHJ blend. The ALO displays the potential to overcome the issues associated with devices that make use of a single OPD with two coloured LEDs, since the power consumption of an ambient light oximeter is lower and it does not need the same level of optoelectronic driving hardware. At present, however, ALOs are limited by the need for the OPDs to be directly facing the light source and motion artifacts are often observed, thus necessitating further development of the ALO concept, and the performance of OPDs utilized in such devices. It should be noted that for a good estimation of blood oxygenation level a high detectivity of 850 nm is required.

It is not surprising that similar to OPV, the replacement of fullerene derivatives with NFAs with absorption extended towards NIR,[7] has opened up a variety of new applications for OPD, such as optical communication and night vision, in addition to the aforementioned medical applications. OPDs based on CO1-4Cl have been recently used for heart-rate monitoring, due to its NIR spectral response of up to 920-960 nm, with a large D* of around 10$_{12}$ Jones, at wavelengths of up to 1010 nm (**Figure 7a-b**).[235] A P3HT:O-IDTBR based OPD has been reported for visible and near-infrared imaging, showing a responsivity value of 0.42 A W$_{-1}$ at 755 nm, similar to a state of the art, commercially available silicon detector.[6] Moreover, this blend processed on a-Si backplanes was able to detect objects under 532 nm and 780 nm light illumination with very low crosstalk between the pixels of the imager (**Figure 7c-e**).

OPDs employing NFAs such as IDFBR and ITIC have been used in combination with a transparent donor polymer (PIF) to demonstrate, for the first time, a multi-channel visible light communication system based on a dual-color inkjet printed array, without the need of any optical filters.[236]
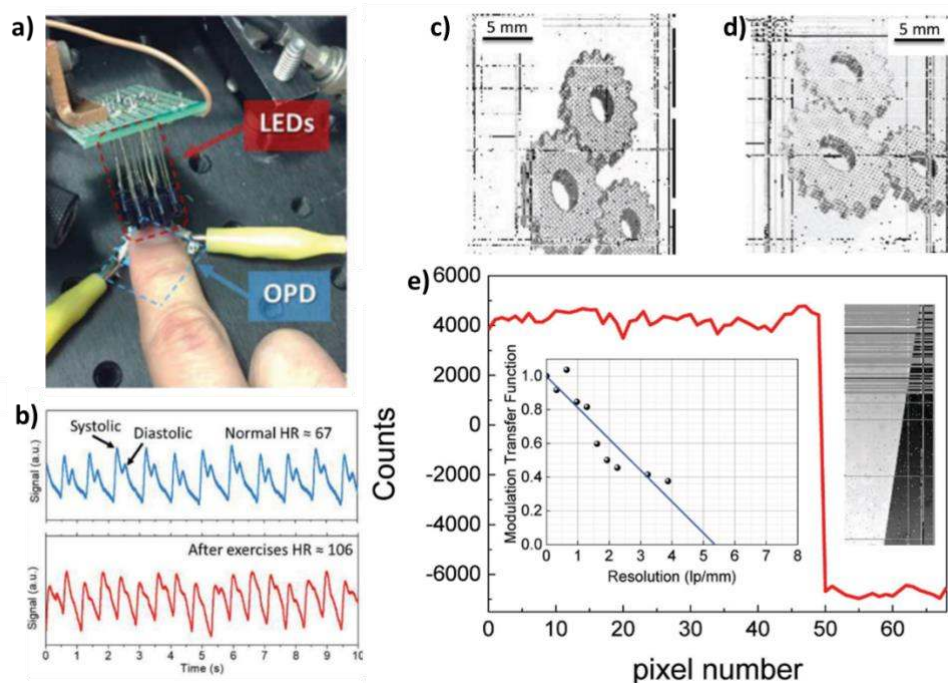

Figure 7. (a) Photograph of the heart rate setup using the OPD. (b) Pulse signal measured from the OPD at normal (upper) and after-exercise (lower) conditions. (c) Visible and (d) infrared shadow cast at 532 and 780 nm, respectively, of a slide showing gears. (e) Image crosstalk shown as the response of a pixel row at a sharp metallic edge under green light illumination. Inset: spatial frequency response of the infrared imager. a-b are reproduced with permission.[235] Copyright 2017, WILEY-VCH Verlag GmbH & Co. KGaA, Weinheim, and c-e are reproduced with permission.[6] Copyright 2017, WILEY-VCH Verlag GmbH & Co. KGaA, Weinheim.

From an engineering perspective, the responsivity of OPDs can be manipulated by employing micrometre thick active layers.[237] PCDTBT and DPP-DTT-based OPDs featured sub-100 nm full-width-half-maximum (FWHM) detection at 700 nm and 950 nm, respectively. This is achieved by inducing the charge collection of weakly absorbed photons close to the electron transporting layer (in a conventional architecture).

A different strategy to narrowing the spectral resolution of OPDs is to employ a D:A BHJ in a resonant optical cavity. In this configuration a weakly absorbing photoactive layer is

sandwiched between two partially reflecting electrodes, which narrow the spectral resonance at specific wavelengths. This concept, however, will not deliver high quality detection for organic semiconductors above-gap wavelengths, where their absorption is strong. In contrast, CT states, which are often unused for photocurrent generation, due to their weak absorption (typically two orders of magnitude lower than singlet absorption of neat materials) can be adopted for NIR detection in resonant optical microcavity devices. Microcavities are formed by fully reflective and partially transmissive silver mirrors, which depending on their thicknesses allow constructive interference for the targeted wavelength and destructive interference for the untargeted wavelength. Zn-phthalocyanine:C_{60} blends,[238] in this configuration, experienced a 41-fold enhancement of EQE at the cavity resonance wavelength and a reduction of FWHMs to 36 nm. These devices delivered over 20% EQEs with photocurrent generation mainly due CT state excitation. Varying the cavity thickness can modulate the resonance wavelength in the CT absorption band from 810 to 1,550 nm.. Recently, solution processed PBTTT:$PC_{61}BM$ blends achieved an FWHM of 14 nm along with EQEs higher than 20% at 960 nm, which is more than 300 nm below the optical gap of the donor polymer.[239] As a proof-of-concept, doctor bladed OPD devices were coated with a thickness wedge to construct a miniaturized spectrometer for wavelength between 700 and 1100 nm (**Figure 8a-b**).
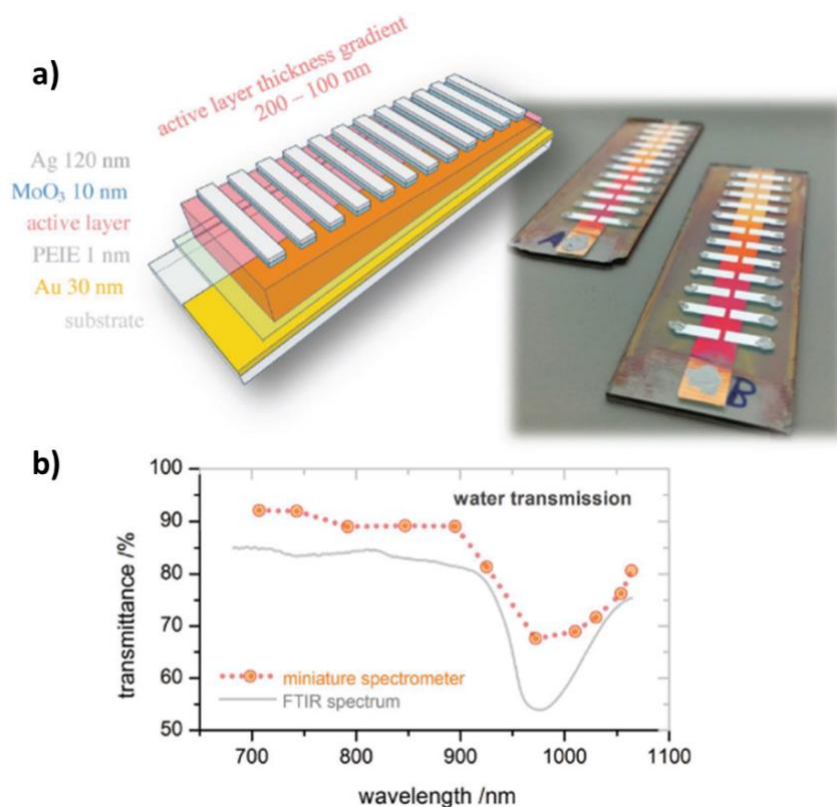
Figure 8. (a) Schematic and a photograph of NIR spectrometer with a thickness-wedged PBTTT:PC$_{61}$BM layer in a metal–metal cavity. (b) Water transmittance spectrum measured by the PBTTT:PC$_{61}$BM spectrometer in comparison to a spectrum measured by a commercial Fourier transform infrared spectrometer. Reproduced with permission.[239] Copyright 2017, WILEY-VCH Verlag GmbH & Co. KGaA, Weinheim.

We anticipate that the use of the BHJ in OPD technologies has the potential to face similar trajectories of growth of OPV. The development of novel materials, as well as device engineering, coupled with a better understanding of the device physics, can make this technology a very promising candidate for the detection of spectral regions which currently is dominated by inorganic counterparts. Moreover, the defined absorption profiles, often exhibited by organic semiconductors, can allow narrow-band detection, which is not currently possible in the broad-band state-of-the-art devices, without the use of filters.

6. Bulk Heterojunctions in Photocatalytic Applications

Organic semiconductors are also increasingly being employed for photocatalytic applications. Organic photocatalysts have been developed to drive a wide range of redox reactions including

synthetic organic transformations,[240–242] degradation of organic pollutants[243,244] and reduction of CO_2 to form value-added chemicals such as CO, CH_4, and CH_3OH.[245,246] However, the reaction that has received the most interest is photocatalytic water splitting to generate H_2 and it is primarily in this context that the use of organic bulk heterojunctions in photocatalytic applications will be discussed.
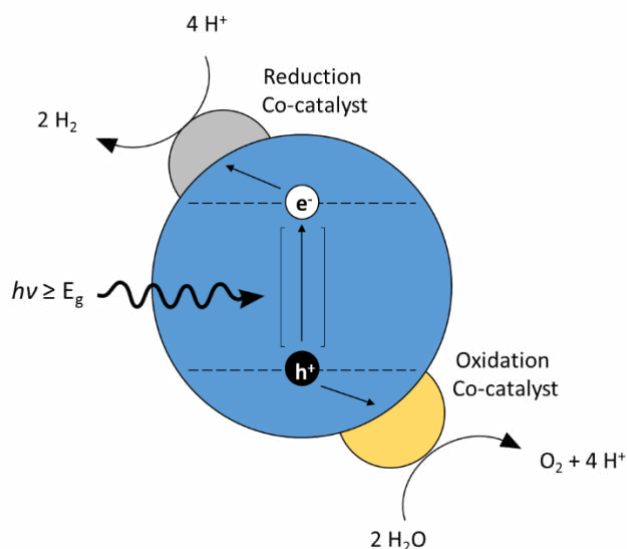

Figure 9. Schematic illustration of the main processes that enable photocatalytic solar to chemical energy conversion. Photocatalytic overall water-splitting is used as an example reaction.

Photocatalysts are materials that absorb light and convert it to photogenerated charges that can drive reductions and oxidations on their surface. Photocatalysts rely on the same fundamental photon to charge carrier conversion processes (light absorption followed by charge separation and charge transport, Figures 1 and 2) as solar cells, but do not have electrodes to extract charges. Instead, photogenerated electrons and holes are extracted at catalytic sites on the photocatalyst surface, which may be inherently present on the semiconductor or added in the form of additional co-catalysts such as transition metal or metal oxide nanoparticles (NPs).[247–249] Photogenerated electrons and holes are then transferred from their respective catalytic sites to oxidants and reductants in the surrounding matrix (**Figure 9**). If the overall redox reaction has a positive ΔG, then the photocatalyst can convert light to chemical energy that is stored in the

reaction products. Using photocatalysts to convert solar energy to such "solar fuels" in this way is highly desirable because it would allow solar energy to be stored when it is abundant and subsequently supplied to users on demand. A mechanism for balancing the intermittency of solar energy such as this is essential to enable it to provide power on a scale commensurate with that currently supplied by fossil fuels.[250]

Most stable photocatalysts developed to date for both single particle systems and Z-schemes have been based on semiconductors with wide and difficult to tune bandgaps such as TiO_2, $SrTiO_3$ and carbon nitrides (CN_xH_y).[251–257] Due to their wide bandgaps, these semiconductors are almost exclusively active at UV wavelengths (<400 nm) that constitute <5% of the solar spectrum (**Figure 10a**).[258] This fundamentally limits the solar conversion efficiency of both single photocatalysts and Z-schemes based on these semiconductors below what is required for many practical solar fuels applications. For example, it has been estimated that a solar to hydrogen efficiency (η_{STH}) of 5-10% would be required to produce hydrogen at the United States Department of Energy's targeted cost of \$2.00–\$4.00 kg^{-1},[259] which is difficult or impossible to achieve with photocatalysts that have little or no activity at wavelengths above 500 nm (**Figure 10b**). This has stimulated interest in fabricating photocatalysts from organic semiconductors which can be synthetically tuned to have narrower bandgaps while ensuring that their energy levels are suitably aligned to drive their respective half-reactions.
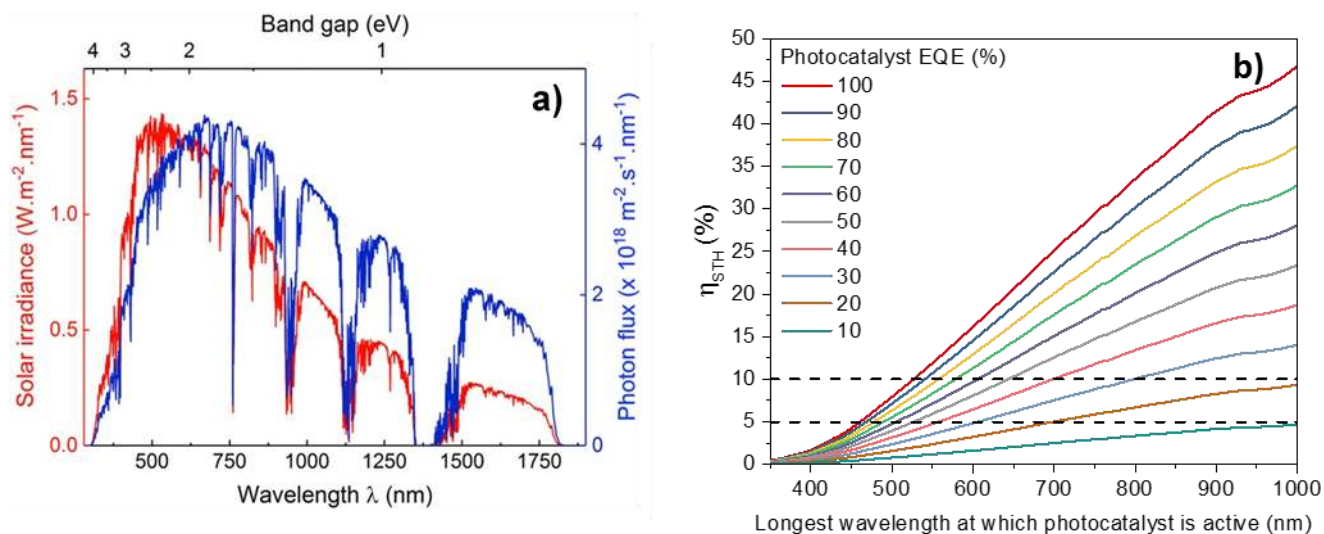
Figure 10. (a) AM1.5 solar spectrum. Reproduced with permission.[260] Copyright 2017, WILEY-VCH Verlag GmbH & Co. KGaA, Weinheim, and (b) Relationship between the STH conversion efficiency and maximum photon wavelengths available for photocatalytic one-step overall water splitting. Data are presented for different external quantum efficiencies (EQEs) covering the typical range from 20 to 100%. The dashed lines indicate the maximum operable wavelength theoretically required to achieve 5% or 10% STH using photocatalysts with different EQEs. The associated calculations assumed AM1.5G solar irradiance.

The photocatalytic activity of organic semiconductors for hydrogen evolution was first demonstrated in 1985, when the conjugated polymer poly(p-phenylene) was used to drive photocatalytic hydrogen evolution from an aqueous solution containing a variety of sacrificial electron donors.[261] The maximum reported H_2 evolution reaction (HER) rate of 207.5 μmolh^{-1}g^{-1} under broad spectrum irradiation (>290 nm) was low, due to the 2.9 eV bandgap of poly(p-phenylene) which limited its photocatalytic activity to wavelengths <430 nm, and its low internal quantum efficiency even at these high energy wavelengths. Since this first report, major efforts have been made to both extend the active wavelength range of organic photocatalysts, and to improve their quantum efficiency. Visible light activity was achieved by narrowing the semiconductor bandgap through molecular design. Incorporating extended aromatic units and heterocycles with stabilized quinoid resonance structures into semiconductor backbones narrowed their bandgaps by extending the π-conjugation length, while the copolymerization of electron rich donor units with electron deficient acceptor units broadened absorption and further

narrowed the optical bandgap through molecular orbital hybridization.[8,262–268] However, the maximum external quantum efficiencies (EQEs) of photocatalysts fabricated from the bulk semiconductors remained mostly below 1%, primarily due to inefficient charge separation within the bulk semiconductors.[269,270] As discussed above, organic semiconductors have high exciton binding energies and typically require a heterojunction to split charges. Therefore, in photocatalysts comprising of a single organic semiconductor, only the excitons generated within the exciton diffusion length from the semiconductor/electrolyte, semiconductor/gas, or semiconductor/co-catalyst heterojunctions at the semiconductor surface can dissociate into free charges that are able to drive photocatalytic redox reactions.

Numerous strategies were therefore developed to optimize these interfaces in order to improve exciton dissociation. Designing the co-catalyst loading method to minimize the size of the loaded co-catalyst particles maximizes the semiconductor/co-catalyst interfacial area, as well as the co-catalyst surface area available to drive the desired redox half-reaction. This improves co-catalyst utilization and can enhance quantum efficiency by enabling more efficient exciton dissociation at the semiconductor/co-catalyst interface.[271–275] At the semiconductor/electrolyte or semiconductor/gas interfaces, exciton dissociation can occur by reductive or oxidative quenching of the photoexcited semiconductor by hole or electron "scavengers" in the surrounding matrix.[276–278] Making the semiconductor surface more accessible to these scavengers can therefore improve the EQE of the photocatalyst by increasing the fraction of excitons that are dissociated by a scavenger. Increasing the photocatalyst surface area by processing bulk semiconductors into nanoparticles (NPs) or nanofibers is a simple and commonly employed strategy to increase their EQE.[9,248,249,268,279–283] Other strategies include designing porous semiconductors such as conjugated microporous polymers and covalent organic frameworks (COFs) which can allow ingress of hole or electron scavengers into the semiconductor pores.[8,284–286] If the photocatalyst needs to operate in a liquid matrix, efficient wetting of the pores by the solvent/scavenger solution is essential to maximize efficiency.[284,287]

These factors are exemplified by a recent study in which Pt loaded linear polymers and COFs containing hydrophilic sulfone units were used as photocatalysts for hydrogen evolution from an aqueous solution containing the hole scavenger ascorbic acid.[284] The 5 to 7 times enhancement in HER rate of the COFs compared to their linear polymer analogues was likely influenced by the increased porosity of the COFs. Furthermore, it was demonstrated that increasing the concentration of hydrophilic sulfone units in the COF improves water adsorption, and this was correlated with higher H_2 evolution rates.[284] Charge generation at the semiconductor surface can also be promoted by sensitization of the semiconductor with a suitable dye.[284,288,289] If the energy levels of the dye and the semiconductor are suitably aligned, electron transfer occurs from the LUMO of the photoexcited dye to the LUMO of the semiconductor. The photogenerated hole remains in the dye molecule HOMO and can be extracted by a suitable hole scavenger or redox mediator in the electrolyte. An added benefit of dye sensitization is that the bandgaps of the dye and the semiconductor can be tuned to have complementary absorptions. This allows the dye sensitized photocatalyst to absorb more of the solar spectrum, which can lead to increased photocatalytic efficiency.[284,289]

The strategies mentioned above are effective at increasing charge separation at the semiconductor surface. However, they do not address the problem of inefficient intrinsic charge generation in the organic semiconductor bulk. Instead, it is also possible to utilize type-II offsets in order to drive exciton scission, with bulk heterojunctions providing a high interfacial area for excitons to be converted into free charge carriers, which can then be used to drive chemical oxidation and reductions. Recently, Pt loaded NPs formed via nanoprecipitation from blends of wide bandgap conjugated polymers were used as photocatalysts for H_2 evolution.[290,291] The highest performing blend consisted of the donor polymer poly [(9,9- dioctylfluorene-2,7-diyl)-alt-(triphenylamine-. 4,4'-diyl)] (PF8TPA) combined with the acceptor polymer Poly(9,9-dioctylfluorene-alt-difluorobenzothiadiazole) (F8dfBT). The blend NPs achieved a HER rate of 7.06 mmolh-1g-1, which is 2.5 times greater than a mixture of NPs formed from the individual

semiconductors. This increase in activity was attributed to exciton separation at the polymer/polymer heterojunction.
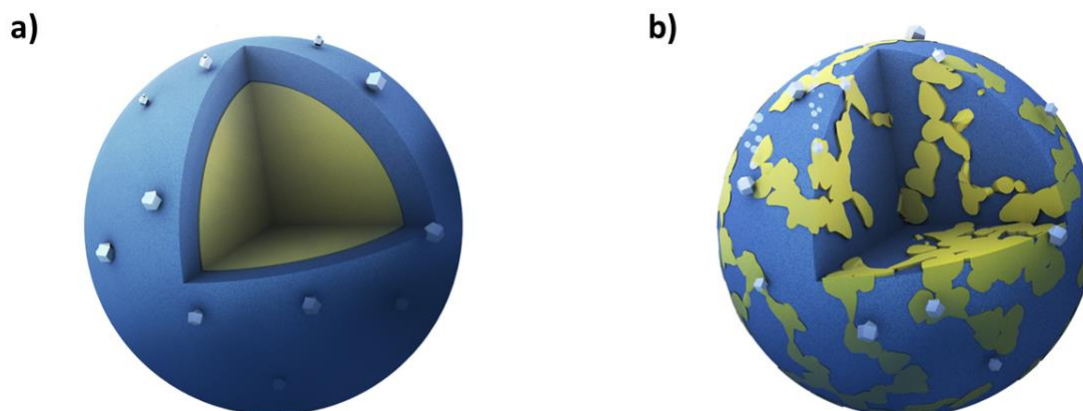

Figure 11. Illustration of heterojunction nanoparticle morphologies. (a) core-shell structure and (b) intermixed heterojunction structure. The silver particles represent the Pt co-catalyst.

Building on these initial results, we recently used the concept of the BHJ to fabricate H_2 evolution photocatalyst NPs from a blend of the donor polymer PTB7-Th and the small molecule non-fullerene acceptor EH-IDTBR. The resulting optimized photocatalysts achieved a HER rate of over 64 mmolh^{-1}g^{-1}; over 20 times that of the individual semiconductors.[9] The activity enhancement was attributed to the internal BHJ that enhances exciton dissociation in the NP bulk, leading to greatly enhanced photocatalytic activity compared to single component NPs, or core-shell morphologies. Control of the heterojunction morphology was critical to maximizing the HER rate, and was achieved by varying the stabilizing surfactant employed during the miniemulsion NP fabrication process.[9,264,292] It was found that in order to avoid the commonly observed,[293] but unfavourable, core-shell heterojunction morphology (**Figure 11a**) it was necessary to tune the interfacial tensions of the donor and the acceptor semiconductors with respect to the surrounding aqueous phase such that they were equal to each other, by carefully selecting the appropriate surfactant. This removed the driving force for the preferential segregation of one component to the NP core, and resulted in an intermixed BHJ morphology with both donor and acceptor domains at the NP surface (**Figure 11b**). The significance of this

control of the heterojunction morphology is that in a core-shell heterojunction NP, one charge carrier species (either electrons or holes) will be trapped within the NP, whereas in a BHJ NP the efficient extraction of both photogenerated holes (by ascorbic acid) and electrons (by the Pt co-catalyst) is possible. As a result, an increased HER rate was achieved, by an order of magnitude in comparison to the core-shell NPs.[9] This approach offers significant promise as an alternative solar technology, making use of known organic semiconductor design, in addition to well understood thermodynamics and photophysics from OPV research, in order to convert solar energy into easily stored chemical fuels. The application of this knowledge from BHJ solar cells to organic photocatalysts provides an opportunity to significantly improve the performance of hydrogen production systems, as well as offer opportunities to potentially convert CO_2 and waste feedstocks into value added products in the future too.

7. Conclusions and Outlook

The evolution of the heterojunction from planar bilayers to mixed BHJs has afforded significant improvements in the performance of OPV devices over the last forty years. The inherent limitations of single component and bilayer organic semiconductor devices, such as poor exciton dissociation, limited photon harvesting and high recombination losses, can be largely overcome in an optimized BHJ active layer, resulting in improvements in the J_{SC} and FF of devices, in particular. With current state-of-the-art PCEs at 18%, for binary blends, OPVs are rapidly emerging as a competitive solar cell technology, rendering them a viable option for commercialization. Selective tuning of the organic semiconductor molecular structure has been used in order to control their energetic offset, complementary light absorption and formation of an interpenetrating nanoscale morphology. This has played a significant role in the great strides made in BHJ solar cells. Moreover, a thorough understanding of the underpinning thermodynamic driving forces in creating BHJs has defined semiconductor design strategies and has highlighted the role of miscibility in the thermal stability of such blends. This still must

be addressed in order to produce solar cells with comparable lifetimes to their inorganic counterparts. Additionally, a deeper understanding of the photophysics of BHJ solar cells, particularly concerning CT states, has led to an evolving picture of the energetic requirements needed in an optimal BHJ solar cell.

Despite the significant progress made in OPV, the BHJ can also offer unique opportunities in alternative organic electronic technologies, such as photodetectors and organic photocatalytic systems. Many of the current OPD devices make use of blends that were previously reported in organic solar cells, therefore utilizing similar chemical design and device engineering strategies may afford lower dark currents, and thus greater sensitivity. Additionally, the use of BHJs in organic photocatalysts provides an exciting opportunity to develop organic semiconductor-based solar fuel technologies. Careful control over the interfacial tension and solubility of semiconductor components can allow BHJ morphology to form in the nanoparticles, which enhances the separation of excitons into free charges and allows both photogenerated electrons and holes to reach the surface, where they can be utilized in oxidation and reduction reactions. In such systems, solar energy can be converted directly into chemical fuels, which can be easily stored, and a vast range of useful chemical reactions can be exploited.

Figure 11 was created by Heno Hwang, scientific illustrator at King Abdullah University of Science and Technology (KAUST).

Received: ((will be filled in by the editorial staff))
Revised: ((will be filled in by the editorial staff))
Published online: ((will be filled in by the editorial staff))

References

[1]   V. Y. Merritt, H. J. Hovel, *Appl. Phys. Lett.*, **1976**, *29*, 414.

[2]   Q. Liu, Y. Jiang, K. Jin, J. Qin, J. Xu, W. Li, J. Xiong, J. Liu, Z. Xiao, K. Sun, S. Yang, X. Zhang, L. Ding, *Sci. Bull.*, **2020**, *65*, 272-275.

[3]   N. Thejo Kalyani, S. J. Dhoble, *Renew. Sust. Energ. Rev.* **2012**, *16*, 2696-2723.

[4]   A. F. Paterson, S. Singh, K. J. Fallon, T. Hodsen, Y. Han, B. C. Schroeder, H. Bronstein, M. Heeney, I. McCulloch, T. D. Anthopoulos, *Adv. Mater.*, **2018**, *30*, 1801079.

[5]   M. Moser, J. F. Ponder Jr., A. Wadsworth, A. Giovannitti, I. McCulloch, *Adv. Funct. Mater.* **2018**, *29*, 1807033

[6]   N. Gasparini, A. Gregori, M. Salvador, M. Biele, A. Wadsworth, S. Tedde, D. Baran, I. McCulloch, C. J. Brabec, Adv. Mater. Technol. **2018**, *3*, 1800104.

[7]   J. Lee, S. J. Ko, H. Lee, J. Huang, Z. Zhu, M. Seifrid, J. Vollbrecht, V. V. Brus, A. Karki, H. Wang, K. Cho, T. Q. Nguyen, G. C. Bazan, *ACS Energy Lett.*, **2019**, *4*, 1401-1409.

[8]   R. S. Sprick, J. X. Jiang, B. Bonillo, S. Ren, T. Ratvijtvech, P. Guiglion, M. A. Zwijnenburg, D. J. Adams, A. I. Cooper, *J. Am. Chem. Soc.*, **2015**, *137*, 3265-3270.

[9]   J. Kosco, M. Bidwell, H. Cha, T. Martin, C. T. Howells, M. Sachs, D. H. Anjum, S. Gonzalez Lopez, L. Zou, A. Wadsworth, W. Zhang, L. Zhang, J. Tellam, R. Sougrat, F. Laquai, D. M. DeLongchamp, J. R. Durrant, I. McCulloch, *Nat. Mater.*, **2020**, https://doi.org/10.1038/s41563-019-0591-1.

[10]   A. K. Ghosh, T. Feng, *J. Appl. Phys.*, **1978**, *49*, 5982.

[11]   S. Barth and H. Bassler, Phys. Rev. Lett., **1997**, *79*, 4445–4448

[12]   G. Dennler, M. C. Scharber and C. J. Brabec, Adv. Mater., **2009**, *21*, 1323–1338.

[13]   J. L. Brédas, D. Beljonne, V. Coropceanu, J. Cornil, *Chem. Rev.*, **2004**, *104*, 4971–5004.

[14]   J. Liu, S. Chen, D. Qian, B. Gautam, G. Yang, J. Zhao, J. Bergqvist, F. Zhang, W. Ma, H. Ade, O. Inganäs, K. Gundogdu, F. Gao, H. Yan, *Nat. Energy*, **2016**, *1*, 16089.

[15]   D. Baran, T. Kirchartz, S. Wheeler, S. D. Dimitrov, M. Abdelsamie, J. Gorman, R. S. Ashraf, S. Holliday, A. Wadsworth, N. Gasparini, P. Kaienburg, H. Yan, A. Amassian, C. J. Brabec, J. R. Durrant, I. McCulloch, *Energy Environ. Sci.* **2016**, *9*, 3783-3793.

[16]   P. Cheng, M. Zhang, T. K. Lau, Y. Wu, B. Jia, J. Wang, C. Yan, M. Qin, Z. Lu, X. Zhan, *Adv. Mater.* **2017**, *29*, 1605216.

[17]   X. Y. Zhu, *J. Phys. Chem. Lett.* **2014**, *5*, 2283-2288.

[18]   D. Cahen, A. Kahn, *Adv. Mater*. **2003**, *15*, 271−277.

[19]   W. Chen, T. Xu, F. He, W. Wang, C. Wang, J. Strzalka, Y. Liu, J. Wen, D. J. Miller, J. Chen, K. Hong, L. Yu, S. B. Darline, *Nano Lett*. **2011**, *11*, 3707−3713.

[20]   A. Jailaubekov, A. P. Willard, J. R. Tritsch, W. L. Chan, N. Sai, R. I. Gearba, L. G. Kaake, K. J. Williams, K. Leung, P. J. Rossky, X. Y. Zhu, *Nat. Mater*. **2013**, *12*, 66-73.

[21]   A. B. Gregg, *J. Phys. Chem. Lett*. **2011**, *2*, 3013−3015.

[22]   D. R. Kozub, K. Vakhshouri, S. V. Kesava, C. Wang, A. Hexemer and E. D. Gomez, *Chem. Commun*., **2012**, *48*, 5859.

[23]   G. J. Hedley, A. J. Ward, A. Alekseev, C. T. Howells, E. R. Martins, L. A. Serrano, G. Cooke, A. Ruseckas and I. D. W. Samuel, *Nat. Commun*., **2013**, *4*, 2867.

[24]   C. W. Tang, *Appl. Phys. Lett*. **1986**, *48*, 183.

[25]   K. L. Mutolo, E. I. Mayo, B. P. Rand, S. R. Forrest, M. E. Thompson, *J. Am. Chem. Soc*. **2006**, *128*, 8108-8109.

[26]   C. F. Lin, S. W. Liu, C. C. Lee, J. C. Hunag, W. C. Su, T. L. Chiu. C. T. Chen, J. H. Lee, *Sol. Energy Mater. Sol. Cells*, **2012**, *103*, 69-75.

[27]   K. Yao, J. J. Intemann, H. L. Yip, P. W. Liang, C. Y. Chang, Y. Zang, Z. Li, Y. Chen, A. K. Y. Jen, *J. Mater. Chem. C*, **2014**, *2*, 416.

[28]   A. Mozer, S. Sariciftci, *C. R. Chimie*, **2006**, *9*, 568.

[29]   V. S. Gevaerts, L. J. A. Koster, M. M. Wienk, R. A. Janssen, *ACS Appl. Mater. Interfaces*, **2011**, *3*, 3252-3255.

[30]   G. Brotas, J. Farinhas, Q. Ferreira, J. Morgado, A. Charas, *Synth. Met.* **2012** *162*, 2052-2058.

[31]   J. Rumer, I. McCulloch, *Mater. Today*, **2015**, *8*, 425.

[32]   M. M. Wienk, J. M. Kroon, W. J. H. Verhees, J. Knol, J. C. Hummelen, P. A. Van Hal, R. A. J. Janssen, *Angew. Chem. Int. Ed.* **2003**, *42*, 3371-3375.

[33]   W. Ma, C. Yang, X. Gong, K. Lee, A. J. Heeger, *Adv. Funct. Mater.* **2005**, *15*, 1617.

[34]   I. Kang, H. J. Yun, D. S. Chung, S. K. Kwon, Y. H. Kim, *J. Am. Chem. Soc.* **2013**, *135*, 14896-14899.

[35]   T. Lei, J. H. Dou, J. Pei, *Adv. Mater.* **2012**, *24*, 6457-6461.

[36]   C. H. Wu, C. C. Chueh, Y. Y. Xi, H. L. Zhong, G. P. Gao, Z. H. Wang, L. D. Pozzo, T. C. Wen and A. K. Y. Jen, *Adv. Funct. Mater*. **2015**, *25*, 5326–5332.

[37]   C. J. Brabec, M. Heeney, I. McCulloch, J. Nelson, *Chem. Soc. Rev.* **2011**, *40*, 1185-1199.

[38]   L. Ye, H. Hu, M. Ghasemi, T. Wang, B. A. Collins, J. H. Kim, K. Jiang, J. H. Carpenter, H. Li, Z. Li, T. McAfee, J. Zhao, X. Chen, J. L. Y. Lai, T. Ma, J. L. Brédas, H. Yan, H. Ade, *Nat. Mater.* **2018**, *17*, 253-260.

[39]   J. A. Bartelt, Z. M. Beiley, E. T. Hoke, W. R. Mateker, J. D. Douglas, B. A. Collins, J. R. Tumbleston, K. R. Graham, A. Amassian, H. Ade, J. M. J. Fréchet,M. F. Toney, M. D. McGehee, *Adv. Energy Mater.* **2013**, *3*, 364-374.

[40]   S. Mukherjee, C. M. Proctor, G. C. Bazan, T. Q. Nguyen, H. Ade, *Adv. Energy Mater.* **2015**, *5*, 1500877.

[41]   T. M. Burke, M. D. McGehee, *Adv. Mater.* **2014**, *26*, 1923-1928.

[42]   X. Du, T. Heumueller, W. Gruber, A. Classen, T. Unruh, N. Li, C. J. Brabec, *Joule*, **2019**, *3*, 215-226.

[43] M. Campoy-Quiles, T. Ferenczi, T. Agostinelli, P. G. Etchegoin, Y. Kim, T. D. Anthopoulos, P. N. Stavrinou, D. D. C. Bradley, J. Nelson, *Nat. Mater*. **2008**, *7*, 158–164.

[44] S. R. Dupont, M. Oliver, F. C. Krebs, R. H. Dauskardt, *Sol. Energy Mater. Sol. Cells*, **2012**, *97*, 171–175.

[45] M. Ghasemi, H. Hu, Z. Peng, J. J. Rech, I. Angunawela, J. H. Carpenter, S. J. Stuard, A. Wadsworth, I. McCulloch, W. You, H. Ade, *Joule*, **2019**, *3*, 1328-1348.

[46] N. Li, J. D. Perea, T. Kassar, M. Richter, T. Heumueller, G. J. Matt, Y. Hou, N. S. Güldal, H. Chen, S. Chen, S. Langner, M. Berlinghof, T. Unruh, C. J. Brabec, *Nat. Commun.* **2017**, *8*, 14541.

[47] Y. He, Y. Li, *Phys. Chem. Chem. Phys*. **2011**, *13*, 1970–1983.

[48] X. Yang, J. Loos, S. Veenstra, W. J. H. Verhees, M. M. Wienk, J. M. Kroon, M. Michels, R. A. J. Janssen, *Nano Lett*. **2005**, *5*, 579–583.

[49] F. L. Zhang, M. Johansson, M. R. Andersson, J. C. Hummelen, O, Inganäs, *Synth. Met.* **2003**, *137*, 1401-1402.

[50] N. S. Sariciftci, *Mater. Today*, **2004**, *25*, 39.

[51] Y. Kim, S. Cook, S. M. Tuladhar, S. A. Choulis, J. Nelson, J. R. Durrant, D. D. C. Bradley, M. Giles, I. McCulloch, C. S. Ha, M. Ree, *Nat. Mater*. **2006**, *5*, 197.

[52] F. Padinger, R. S. Rittberger, N. S. Sariciftci, *Adv. Funct. Mater*. **2003**, *13*, 85.

[53] J. Yao, T. Kirchartz, M. S. Vezie, M. A. Faist, W. G. Zhicai, H. Wu, J. Troughton, T. Watson, D. Bryant, J. Nelson, *Phys. Rev. Appl*. **2015**, *4*, 014020.

[54] J. P. Sun, C. Cui, H. Q. Wang, Y. Li, *Adv. Energy Mater*. **2011**, *1*, 1058.

[55] X. Guo, C. Cui, M. Zhang, L. Huo, L. Huang, J. Hou, Y. Li, *Energy Environ. Sci*. **2012**, *5*, 7943.

[56] S. H. Park, A. Roy, S. Beaupré, S. Cho, N. Coates, J. S. Moon, D. Moses, M. Leclerc, K. Lee, A. J. Heeger, *Nat. Photonics*, **2009**, *3*, 297-303.

[57] Z. He, B. Xiao, F. Liu, Y. Yang, S. Xiao, C. Wang, T. P. Russell, Y. Cao, N*at. Photonics*, **2015**, *9*, 174–179.

[58] Y. Liu, J. Zhao, Z. Li, C. Mu, W. Ma, H. Hu, K. Jiang, H. Lin, H. Ade, H. Yan, *Nat. Commun*. **2014**, *5*, 5293.

[59] J. Zhao, Y. Li, G. Yang, K. Jiang, H. Lin, H. Ade, W. Ma, H. Yan, *Nat. Energy*, **2016**, *1*, 15027.

[60] J. Peet, J. Y. Kim, N. E. Coates, W. L. Ma, D. Moses, A. J. Heeger, G. C. Bazan,*Nat. Mater.* **2007**, *6*, 497-500.

[61] F. C. Chen, H. C. Tseng, C. J. Ko, *Appl. Phys. Lett.* **2008**, *92*, 103316.

[62] J. Peet, E. Brocker, Y. Xu, G. C. Bazan, *Adv. Mater.* B2008**, *20*, 1882-1885.**

[63] B. J. Tremolet de Villers, K. A. O'Hara, D. P. Ostrowski, P. H. Biddle, S. E. Shaheen, M. L. Chabinyc, D. C. Olson, N. Kopidakis, *Chem. Mater*. **2016**, *28*, 876−884

[64] X. Zhao, J. Zhao, R. Wu, D. Liu, G. Wang, P. Li, L. Chen, L. Zhu, B. Ding, Q. Song, *Org. Electron.* 2017, **49**, 226.

[65] A. Sharenko, C. M. Proctor, T. S. van der Poll, Z. B. Henson, T.Q. Nguyen, G. C. Bazan, *Adv. Mater*. **2013**, *25*, 4403–4407.

[66] Y. Lin and X. Zhan, *Adv. Energy Mater.* **2015**, *5*, 1501063.

[67] R. Singh, J. Lee, M. Kim, P. E. Keivanidis, K. Cho, *J. Mater. Chem. A* **2017**, *5*, 210-220.

[68] C.H. Wu, C.C. Chueh, Y.Y. Xi, H.L. Zhong, G.P. Gao, Z.H. Wang, L. D. Pozzo, T.C. Wen, A. K.Y. Jen, *Adv. Funct. Mater*. **2015**, *25*, 5326–5332.

[69] Y. Duan, X. Xu, H. Yan, W. Wu, Z. Li, Q. Peng, *Adv. Mater*. **2017**, *29*, 1605115.

[70] S. Holliday, R. S. Ashraf, C. B. Nielsen, M. Kirkus, J. A. Röhr, C.H. Tan, E. Collado-Fregoso, A.C. Knall, J. R. Durrant, J. Nelson, I. McCulloch, *J. Am. Chem. Soc*. **2015**, *137*, 898–904.

[71] S. Holliday, R. S. Ashraf, A. Wadsworth, D. Baran, S. A. Yousef, C. B. Nielsen, C. H. Tan, S. D. Dimitorv, Z. Shang, N. Gasparini, M. Alamoudi, F. Laquai, C. J. Brabec, A. Salleo, J. R. Durrant, I. McCulloch, *Nat. Commun.* **2016**, *7*, 11585.

[72] A. Wadsworth, Z. Hamid, M. Bidwell, R. S. Ashraf, J. I. Khan, D. H. Anjum, C. Cendra, J. Yan, E. Rezasoltani, A. A. Y. Guilbert, M. Azzouzi, N. Gasparini, J. H. Bannock, D. Baran, H. Wu, J. C. de Mello, C. J. Brabec, A. Salleo, J. Nelson, F. Laquai, I. McCulloch, *Adv. Energy Mater.* **2018**, *8*, 1801001.

[73] D. Baran, N. Gasparini, A. Wadsworth, C. H. Tan, N. Wehbe, X. Song, Z. Hamid, W. Zhang, M. Neophytou, T. Kirchartz, C. J. Brabec, J. R. Durrant, I. McCulloch, *Nat. Commun.*, **2018**, *9*, 2059.

[74] Y. Lin, J. Wang, Z. G. Zhang, H. Bai, Y. Li, D. Zhu, X. Zhan, *Adv. Mater.* **2015**, *27*, 1170–1174.

[75] Z. Li, K. Jiang, G. Yang, J. Y. L. Lai, T. Ma, J. Zhao, W. Ma, H. Yan, *Nat. Commun.* **2016**, *7*, 13094.

[76] Y. Yang, Z.G. Zhang, H. Bin, S. Chen, L. Gao, L. Xue, C. Yang, Y. Li, *J. Am. Chem. Soc.* **2016**, *138*, 15011–15018.

[77] B. Jia, Y. Wu, F. Zhao, C. Yan, S. Zhu, P. Cheng, J. Mai, T. K. Lau, X. Lu, C. J. Su, C. Wang, X. Zhan, *Sci. China: Chem.* **2017**, *60*, 257–263.

[78] W. Zhao, S. Li, H. Yao, S. Zhang, Y. Zhang, B. Yang, J. Hou, J. Am. Chem. Soc., 2017, 139, 7148–7151.

[79] S. Li, L. Ye, W. Zhao, S. Zhang, S. Mukherjee, H. Ade, J. Hou, *Adv. Mater.* **2016**, *28*, 9423–9429.

[80] Y. Li, L. Zhong, B. Gautam, H.J. Bin, J.D. Lin, F.P. Wu, Z. Zhang, Z.Q. Jiang, Z.G. Zhang, K. Gundogdu, Y. Li, L.S. Liao, *Energy Environ. Sci.* **2017**, *10*, 1610–1620.

[81]   J. Yuan, Y. Zhang, L. Zhou, G. Zhang, H. L. Yip, T. K. Lau, X. Lu, C. Zhu, H. Peng, P. A. Johnson, M. Leclerc, Y. Cao, J. Ulanski, Y. Li, Y. Zou, *Joule*, **2019**, *3*, 1140-1151.

[82]   A. Karki, J. Vollbrecht, A. L. Dixon, N. Schopp, M. Schrock, G. N. Manjunatha Reddy, T. Q. Nguyen, *Adv. Mater.* **2019**, *31*, 1903868.

[83]   Y. Lin, B. Adilbekova, Y. Firdaus, E. Yengel, H. Faber, M. Sajjas, X. Zheng, E. Yarali, A. Seitkhan, O. M. Bakr, A. El-Labban, U. Schwingenschlögl, V. Tung, I. McCulloch, F. Laquai, T. D. Anthopoulos, *Adv. Mater.* **2019**, *31*, 1902965.

[84]   Q. Liu, Y. Jiang, K. Jin, J. Qin, J. Xu, W. Li, J. Xiong, J. Liu, Z. Xiao, K. Sun, S. Yang, X. Zhang, L. Ding, *Sci. Bull.* **2020**, *65*, 272-275.

[85]   H. Kang, W. Lee, J. Oh, T. Kim, C. Lee, B. J. Kim, *Acc. Chem. Res.* **2016**, *49*, 2424-2434.

[86]   H. Yan, Z. Chen, Y. Zheng, C. Newman, J. R. Quinn, F. Dötz, M. Kastler, A. Facchetti, *Nature*, **2009**, *457*, 679–686.

[87]   J. R. Moore, S. Albert-Seifried, A. Rao, S. Massip, B. Watts, D. J. Morgan, R. H. Friend, C. R. McNeill, H. Sirringhaus, *Adv. Energy Mater.* **2011**, *1*, 230–240.

[88]   M. Schubert, D. Dolfen, J. Frisch, S. Roland, R. Steyrleuthner, B. Stiller, Z. Chen, U. Scherf, N. Koch, A. Facchetti, D. Neher, *Adv. Energy Mater.* **2012**, *2*, 369–380.

[89]   Y. J. Hwang, B. A. E. Courtright, A. S. Ferreira, S. H. Tolbert, S. A. Jenehke, *Adv. Mater.* **2015**, *27*, 4578–4584.

[90]   Y. Guo, Y. Li, O. Awartani, H. Han, J. Zhao, H. Ade, H. Yan, D. Zhao, *Adv. Mater.* **2017**, *29*, 1700309.

[91]   Z. Li, X. Xu, W. Zhang, X. Meng, W. Ma, A. Yartsev, O. Inganäs, M. R. Andersson, R. A. J. Janssen, E. Wang, *J. Am. Chem. Soc.* **2016**, *138*, 10935–10944.

[92]   B. Fan, L. Ying, P. Zhu, F. Pan, F. Liu, J. Chen, F. Huang, Y. Cao, *Adv. Mater.* **2017**, *29*, 1703906.

[93] K. Sun, Z. Xiao, S. Lu, W. Zajaczkowski, W. Pisula, E. Hanssen, J. M. White, R. M. Williamson, J. Subbiah, J. Ouyang, A. B. Holmes, W. W. H. Wong, D. J. Jones, *Nat. Commun*. **2015**, *6*, 6013.

[94] K. Gao, S. B. Jo, X. Shi, L. Nian, M. Zhang, Y. Kan, F. Lin, B. Kan, B. Xu, Q. Rong, L. Shui, F. Liu, X. Peng, G. Zhou, Y. Cao, A. K. Y. Jen, *Adv. Mater*. **2019**, *31*, 1807842.

[95] N. Gasparini, A. Salleo, I. McCulloch, D. Baran, *Nat. Rev. Mater.* **2019**, *4*, 229-242.

[96] L. Zhan, S. Li, T. K. Lau, Y. Cui, X. Lu, M. Shi, C. Z. Li, H. Li, J. Hou, H. Chen, *Energy Environ. Sci.* **2020**, *13*, 635-645.

[97] R. A. Street, D. Davies, P. P. Khlyabich, B. Burkhart, B. C. Thompson, *J. Am. Chem. Soc.* **2013**, *135*, 986-989.

[98] N. Gasparini, S. H. K. Paleti, J. Bertrandie, G. Cai, G. Zhang, A. Wadsworth, X. Lu, H. L. Yip, I. McCulloch, D. Baran, *ACS Energy Lett.* **2020**, *5*, 1371-1379.

[99] R. Yu, H. Yao, Y. Cui, L. Hong, C. He, J. Hou, *Adv. Mater.* **2019**, *31*, 1902302.

[100] T. Yan, J. Ge, T. Lei, W. Zhang, W. Song, B. Fanady, D. Zhang, S. Chen, R. Peng, Z. Ge, *J. Mater. Chem. A*, **2019**, *7*, 25894-25899.

[101] B. A. Collins, E. Gann, L. Guignard, X. He, C. R. McNeill, H. Ade, *J. Phys. Chem. Lett*. **2010**, *1*, 3160.

[102] Y. Kim, S. Cook, S. M. Tuladhar, S. A. Choulis, J. Nelson, J. R. Durrant, D. D. C. Bradley, M. Giles, I. McCulloch, C. S. Ha, M. Ree, *Nat. Mater.* **2006**, *5*, 197.

[103] P. Schilinsky, U. Asawapirom, U. Scherf, M. Biele, C. J. Brabec, *Chem. Mater.* **2005**, *17*, 2175.

[104] A. M. Ballantyne, L. Chen, J. Dane, T. Hammant, F. M. Braun, M. Heeney, W. Duffy, I. McCulloch, D. D. C. Bradley, J. Nelson, *Adv. Funct. Mater.* **2008**, *18*, 2373.

[105] C. H. Woo, B. C. Thompson, B. J. Kim, M. F. Toney, J. M. J. Fréchet, *J. Am. Chem. Soc*. **2008**, *130*, 16324.

[106] A. A. Y. Guilbert, M. Schmidt, A. Bruno, J. Yao, S. King, S. M. Tuladhar, T. Kirchartz, M. I. Alonso, A. R. Goñi, N. Stingelin, S. A. Haque, M. Campoy-Quiles, J. Nelson, *Adv. Funct. Mater.* **2014**, *24*, 6972.

[107] F. C. Jamieson, E. B. Domingo, T. Mccarthy-Ward, M. Heeney, N. Stingelin, J. R. Durrant, *Chem. Sci.* **2012**, *3*, 485.

[108] C. Müller, T. A. M. Ferenczi, M. Campoy-Quiles, J. M. Frost, D. D. C. Bradley, P. Smith, N. Stingelin-Stutzmann, J. Nelson, *Adv. Mater.* **2008**, *20*, 3510.

[109] Z. Fei, F. D. Eisner, X. Jiao, M. Azzouzi, J. A. Röhr, Y. Han, M. Shahid, A. S. R. Chesman, C. D. Easton, C. R. Mcneill, T. D. Anthopoulos, J. Nelson, M. Heeney, *Adv. Mater.* **2018**, *30*, 1705209.

[110] S. Rajaram, R. Shivanna, S. Kumar Kandappa, K. S. Narayan, *J. Phys. Chem. Lett.* **2012**, *3*, 2405.

[111] Y. Liu, J. Y. L. Lai, S. Chen, Y. Li, K. Jiang, J. Zhao, Z. Li, H. Hu, T. Ma, H. Lin, J. Liu, J. Zhang, F. Huang, D. Yu, H. Yan, *J. Mater. Chem. A*, **2015**, *3*, 13632.

[112] C. McDowell, M. Abdelsamie, M. F. Toney, G. C. Bazan, *Adv. Mater.* **2018**, *30*, 1707114.

[113] H. Kang, W. Lee, J. Oh, T. Kim, C. Lee, B. J. Kim, *Acc. Chem. Res.* **2016**, *49*, 2424.

[114] S. Fabiano, Z. Chen, S. Vahedi, A. Facchetti, B. Pignataro, M. A. Loi, *J. Mater. Chem.* **2011**, *21*, 5891.

[115] K. D. Deshmukh, T. Qin, J. K. Gallaher, A. C. Y. Liu, E. Gann, K. O'Donnell, L. Thomsen, J. M. Hodgkiss, S. E. Watkins, C. R. McNeill, *Energy Environ. Sci.* **2015**, *8*, 332.

[116] M. Ghasemi, L. Ye, Q. Zhang, L. Yan, J. H. Kim, O. Awartani, W. You, A. Gadisa, H. Ade, *Adv. Mater.* **2017**, *29*, 1604603.

[117] K. D. Deshmukh, R. Matsidik, S. K. K. Prasad, L. A. Connal, A. C. Y. Liu, E. Gann, L. Thomsen, J. M. Hodgkiss, M. Sommer, C. R. McNeill, *Adv. Funct. Mater.* **2018**, *28*,

1707185.

[118] N. Zhou, A. S. Dudnik, T. I. N. G. Li, E. F. Manley, T. J. Aldrich, P. Guo, H. C. Liao, Z. Chen, L. X. Chen, R. P. H. Chang, A. Facchetti, M. Olvera De La Cruz, T. J. Marks, *J. Am. Chem. Soc*. **2016**, *138*, 1240.

[119] H. Kang, M. A. Uddin, C. Lee, K. H. Kim, T. L. Nguyen, W. Lee, Y. Li, C. Wang, H. Y. Woo, B. J. Kim, *J. Am. Chem. Soc.* **2015**, *137*, 2359.

[120] R. Radbeh, E. Parbaile, J. Boucle, C. Di Bin, A. Moliton, V. Coudert, F. Rossignol, B. Ratier, *Nanotechnology* **2010**, *21*, 035201.

[121] S. Nilsson, A. Bernasik, A. Budkowski, E. Moons, *Macromolecules* **2007**, *40*, 8291.

[122] B. A. Collins, Z. Li, J. R. Tumbleston, E. Gann, C. R. McNeill, H. Ade, *Adv. Energy Mater.* **2013**, *3*, 65.

[123] J. A. Bartelt, J. D. Douglas, W. R. Mateker, A. El Labban, C. J. Tassone, M. F. Toney, J. M. J. Fréchet, P. M. Beaujuge, M. D. McGehee, *Adv. Energy Mater.* **2014**, *4*, 1301733.

[124] Y. Gu, C. Wang, T. P. Russell, *Adv. Energy Mater.* **2012**, *2*, 683.

[125] Q. Liang, X. Jiao, Y. Yan, Z. Xie, G. Lu, J. Liu, Y. Han, *Adv. Funct. Mater.* **2019**, *29*, 1807591.

[126] J. Peet, C. Soci, R. C. Coffin, T. Q. Nguyen, A. Mikhailovsky, D. Moses, G. C. Bazan, *Appl. Phys. Lett.* **2006**, *89*, 252105.

[127] Y. Yao, J. Hou, Z. Xu, G. Li, Y. Yang, *Adv. Funct. Mater.* **2008**, *18*, 1783.

[128] Y. Kim, S. A. Choulis, J. Nelson, D. D. C. Bradley, S. Cook, J. R. Durrant, *J. Mater. Sci.* **2005**, *40*, 1371.

[129] H. Cha, G. Fish, J. Luke, A. Alraddadi, H. H. Lee, W. Zhang, Y. Dong, S. Limbu, A. Wadsworth, I. P. Maria, L. Francàs, H. L. Sou, T. Du, J. Kim, M. A. McLachlan, I. McCulloch, J. R. Durrant, *Adv. Energy Mater.* **2019**, *9*, 1901254.

[130] H. Hu, P. C. Y. Chow, G. Zhang, T. Ma, J. Liu, G. Yang, H. Yan, *Acc. Chem. Res.*

2017, *50*, 2519.

[131] Y. Lin, Z. G. Zhang, H. Bai, J. Wang, Y. Yao, Y. Li, D. Zhu, X. Zhan, *Energy Environ. Sci.* **2015**, *8*, 610.

[132] J. L. Wang, K. K. Liu, J. Yan, Z. Wu, F. Liu, F. Xiao, Z. F. Chang, H. B. Wu, Y. Cao, T. P. Russell, *J. Am. Chem. Soc*. **2016**, *138*, 7687.

[133] J. A. Love, C. M. Proctor, J. Liu, C. J. Takacs, A. Sharenko, T. S. van der Poll, A. J. Heeger, G. C. Bazan, T. Q. Nguyen, *Adv. Funct. Mater.* **2013**, *23*, 5019.

[134] Y. Xia, C. Musumeci, J. Bergqvist, W. Ma, F. Gao, Z. Tang, S. Bai, Y. Jin, C. Zhu, R. Kroon, C. Wang, M. R. Andersson, L. Hou, O. Inganäs, I. Inganäs, E. Wang, *J. Mater. Chem. A* **2016**, *4*, 3835.

[135] S. Kouijzer, J. J. Michels, M. van den Berg, V. S. Gevaerts, M. Turbiez, M. M. Wienk, R. A. J. Janssen, M. Van Den Berg, S. Gevaerts, *J. Am. Chem. Soc.* **2013**, *135*, 12057.

[136] Z. Peng, X. Jiao, L. Ye, S. Li, J. J. Rech, W. You, J. Hou, H. Ade, *Chem. Mater.* **2018**, *30*, 3943.

[137] J. Perea, S. Langner, M. Salvador, B. Sanchez-Lengeling, N. Li, C. Zhang, G. Jarvas, J. Kontos, A. Dallos, A. Aspuru-Guzik, C. J. Brabec, *J. Phys. Chem. C* **2017**, *121*, 18153.

[138] P. Wolfer, P. E. Schwenn, A. K. Pandey, Y. Fang, N. Stingelin, P. L. Burn, P. Meredith, *J. Mater. Chem. A* **2013**, *1*, 5989.

[139] C. Muller, J. Bergqvist, K. Vandewal, K. Tvingstedt, A. S. Anselmo, R. Magnusson, M. I. Alonso, E. Moons, H. Arwin, M. Campoy-Quiles, O. Inganäs As, *J. Mater. Chem.* **2011**, *21*, 10676.

[140] N. C. Miller, R. Gysel, C. E. Miller, E. Verploegen, Z. Beiley, M. Heeney, I. McCulloch, Z. Bao, M. F. Toney, M. D. McGehee, *J. Polym. Sci., Part B: Polym. Phys.* **2011**, *49*, 499.

[141] A. M. Ballantyne, T. A. M. Ferenczi, M. Campoy-Quiles, T. M. Clarke, A. Maurano, K. H. Wong, W. Zhang, N. Stingelin-Stutzmann, J. S. Kim, D. D. C. Bradley, J. R.

Durrant, I. Mcculloch, M. Heeney, J. Nelson, S. Tierney, W. Duffy, C. Mueller, P.
Smith, *Macromolecules* **2010**, *43*, 1169.

[142] Z. Hamid, A. Wadsworth, E. Rezasoltani, S. Holliday, M. Azzouzi, M. Neophytou, A.
A. Y. Guilbert, Y. Dong, M. S. Little, S. Mukherjee, A. A. Herzing, H. Bristow, R. J.
Kline, D. M. DeLongchamp, A. A. Bakulin, J. R. Durrant, J. Nelson, I. McCulloch,
Adv. Energy Mater. **2020**, 1903248, https://doi.org/10.1002/aenm.201903248.

[143] W. R. Burghardt, *Macromolecules* **1989**, *22*, 2482.

[144] L. Ye, B. A. Collins, X. Jiao, J. Zhao, H. Yan, H. Ade, *Adv. Energy Mater.* **2018**, *8*,
1703058.

[145] J. Xin, X. Meng, X. Xu, Q. Zhu, H. B. Naveed. W. Ma, *Matter*, **2019**, *1*, 1316.

[146] D. Baran, R. S. Ashraf, D. A. Hanifi, M. Abdelsamie, N. Gasparini, J. A. Röhr, S.
Holliday, A. Wadsworth, S. Lockett, M. Neophytou, C. J. M. Emmott, J. Nelson, C. J.
Brabec, A. Amassian, A. Salleo, T. Kirchartz, J. R. Durrant, I. McCulloch, *Nat. Mater.*
2017, *16*, 363.

[147] J. Martín, D. Cangialosi, N. Stingelin, presented at INFORM, València, March, **2019**.

[148] B. Watts, W. J. Belcher, L. Thomsen, H. Ade, P. C. Dastoor, *Macromolecules* **2009**,
42, 8392.

[149] H. Bin, Y. Yang, Z. G. Zhang, L. Ye, M. Ghasemi, S. Chen, Y. Zhang, C. Zhang, C.
Sun, L. Xue, C. Yang, H. Ade, Y. Li, *J. Am. Chem. Soc.* **2017**, *139*, 5085.

[150] H. Hu, Y. Li, J. Zhang, Z. Peng, L. Ma, J. Xin, J. Huang, T. Ma, K. Jiang, G. Zhang,
W. Ma, H. Ade, H. Yan, *Adv. Energy Mater.* **2018**, *8*, 1800234.

[151] H. Li, Y. Zhao, J. Fang, X. Zhu, B. Xia, K. Lu, Z. Wang, J. Zhang, X. Guo, Z. Wei,
Adv. Energy Mater. **2018**, *8*, 1702377.

[152] S. A. Dowland, M. Salvador, J. Perea, N. Gasparini, S. Langner, S. Rajoelson, H. H.
Ramanitra, B. D. Lindner, A. Osvet, C. J. Brabec, R. C. Hiorns, H. J. Egelhaaf, *ACS
Appl. Mater. Interfaces* **2017**, *9*, 10971.

[153] D. R. Kozub, K. Vakhshouri, L. M. Orme, C. Wang, A. Hexemer, E. D. Gomez, *Macromolecules* **2011**, *44*, 5722.

[154] F. Liu, D. Chen, C. Wang, K. Luo, W. Gu, A. L. Briseno, J. W. P. Hsu, T. P. Russell, *ACS Appl. Mater. Interfaces* **2014**, *6*, 19876.

[155] D. Leman, M. A. Kelly, S. Ness, S. Engmann, A. Herzing, C. Snyder, H. W. Ro, R. J. Kline, D. M. DeLongchamp, L. J. Richter, *Macromolecules* **2015**, *48*, 383.

[156] R. A. Matkar, T. Kyu, *J. Phys. Chem. B* **2006**, *110*, 12728.

[157] P. Rathi, T. M. Huang, P. Dayal, T. Kyu, *J. Phys. Chem. B* **2008**, *112*, 6460.

[158] L. Yu, D. Qian, S. Marina, F. A. A Nugroho, A. Sharma, S. Hultmark, A. I. Hofmann, R. Kroon, J. Benduhn, D. M. Smilgies, K. Vandewal, M. R. Andersson, C. Langhammer, J. Martín, F. Gao, C. Muller, *ACS Appl. Mater. Interfaces* **2019**, *11*, 21766.

[159] Y. Zhang, H. L. Yip, O. Acton, S. K. Kau, F. Huang and A. K. Y. Jen, *Chem. Mater.* **2009**, *21*, 2598.

[160] L. H. Nguyen, H. Hoppe, T. Erb, S. Günes, G. Gobsch, N. S. Sariciftci, *Adv. Funct. Mater.* **2007**, *17*, 1071.

[161] A. Diaz De Zerio Mendaza, A. Melianas, F. A. A. Nugroho, O. Acke, E. Olsson, C. Langhammer, O. Inganäs, C. Uller, *J. Mater. Chem A*, **2017**, *5*, 4156.

[162] S. Bertho, G. Janssen, T. J. Cleij, B. Conings, W. Moons, A. Gadisa, J. D'Haen, E. Goovaerts, L. Lutsen, J. Manca, D. Vanderzande, *Sol. Energy Mater. Sol. Cells*, **2008**, *92*, 753.

[163] T. Kim, J. Choi, H. J. Kim, W. Lee, B. J. Kim, *Macromolecules*, **2017**, *50*, 6861.

[164] W. Shockley, H. J. Queisser, *J. Appl. Phys.* **1961**, *32*, 510.

[165] T. Kirchartz, U. Rau, *J. Appl. Phys.* **2007**, *102*, 104510.

[166] L. Krückemeier, U. Rau, M. Stolterfoht, T. Kirchartz, *Adv. Energy Mater.* **2020**, *10*, 1902573.

[167] S. M. Menke, N. A. Ran, G. C. Bazan, R. H. Friend, *Joule* **2018**, *2*, 25.

[168] J. Yao, T. Kirchartz, M. S. Vezie, M. A. Faist, W. Gong, Z. He, H. Wu, J. Troughton, T. Watson, D. Bryant, J. Nelson, *Phys. Rev. Appl.* **2015**, *4*, 014020.

[169] A. A. Bakulin, A. Rao, V. G. Pavelyev, P. H. M. van Loosdrecht, M. S. Pshenichnikov, D. Niedzialek, J. Cornil, D. Beljonne, R. H. Friend, *Science,* **2012**, *335*, 1340.

[170] M. List, T. Sarkar, P. Perkhun, J. Ackermann, C. Luo, U. Würfel, *Nat. Commun.* **2018**, *9*, 3631.

[171] V. Coropceanu, X. K. Chen, T. Wang, Z. Zheng, J. L. Brédas, *Nat. Rev. Mater.* **2019**, *4*, 689.

[172] K. Vandewal, K. Tvingstedt, A. Gadisa, O. Inganäs, J. V Manca, *Nat. Mater.* **2009**, *8*, 904.

[173] K. Vandewal, S. Albrecht, E. T. Hoke, K. R. Graham, J. Widmer, J. D. Douglas, M. Schubert, W. R. Mateker, J. T. Bloking, G. F. Burkhard, A. Sellinger, J. M. J. Fréchet, A. Amassian, M. K. Riede, M. D. McGehee, D. Neher, A. Salleo, *Nat. Mater.* **2014**, *13*, 63.

[174] K. Vandewal, J. Widmer, T. Heumueller, C. J. Brabec, M. D. McGehee, K. Leo, M. Riede, A. Salleo, *Adv. Mater.* **2014**, *26*, 3839.

[175] J. Benduhn, K. Tvingstedt, F. Piersimoni, S. Ullbrich, Y. Fan, M. Tropiano, K. A. McGarry, O. Zeika, M. K. Riede, C. J. Douglas, S. Barlow, S. R. Marder, D. Neher, D. Spoltore, K. Vandewal, *Nat. Energy* **2017**, *2*, 17053.

[176] M. Azzouzi, J. Yan, T. Kirchartz, K. Liu, J. Wang, H. Wu, J. Nelson, *Phys. Rev. X* **2018**, *8*, 031055.

[177] F. D. Eisner, M. Azzouzi, Z. Fei, X. Hou, T. D. Anthopoulos, T. J. S. Dennis, M. Heeney, J. Nelson, *J. Am. Chem. Soc.* **2019**, *141*, 6362.

[178] D. Qian, Z. Zheng, H. Yao, W. Tress, T. R. Hopper, S. Chen, S. Li, J. Liu, S. Chen, J. Zhang, X. K. Liu, B. Gao, L. Ouyang, Y. Jin, G. Pozina, I. A. Buyanova, W. M. Chen, O. Inganäs, V. Coropceanu, J. L. Bredas, H. Yan, J. Hou, F. Zhang, A. A. Bakulin, F. Gao, *Nat. Mater.* **2018**, *17*, 703.

[179] K. Vandewal, Z. Ma, J. Bergqvist, Z. Tang, E. Wang, P. Henriksson, K. Tvingstedt, M. R. Andersson, F. Zhang, O. Inganäs, *Adv. Funct. Mater.* **2012**, *22*, 3480.

[180] M. E. Ziffer, S. B. Jo, H. Zhong, L. Ye, H. Liu, F. Lin, J. Zhang, X. Li, H. W. Ade, A. K. Y. Jen, D. S. Ginger, *J. Am. Chem. Soc.* **2018**, *140*, 9996.

[181] R. A. Marcus, *J. Phys. Chem.* **1989**, *93*, 3078.

[182] K. R. Graham, G. O. N. Ndjawa, S. M. Conron, R. Munir, K. Vandewal, J. J. Chen, S. Sweetnam, M. E. Thompson, A. Salleo, M. D. McGehee, A. Amassian, *Adv. Energy Mater.* **2016**, 1601211.

[183] Z. Zheng, N. R. Tummala, T. Wang, V. Coropceanu, J. Brédas, *Adv. Energy Mater.* **2019**, *9*, 1803926.

[184] S. Liu, J. Yuan, W. Deng, M. Luo, Y. Xie, Q. Liang, Y. Zou, Z. He, H. Wu, Y. Cao, *Nat. Photonics* **2020**, DOI 10.1038/s41566-019-0573-5.

[185] L. Perdigón-Toro, H. Zhang, A. Markina, J. Yuan, S. M. Hosseini, C. M. Wolff, G. Zuo, M. Stolterfoht, Y. Zou, F. Gao, D. Andrienko, S. Shoaee, D. Neher, *Adv. Mater.* **2020**, 1906763.

[186] N. Gasparini, M. Salvador, T. Heumueller, M. Richter, A. Classen, S. Shrestha, G. J. Matt, S. Holliday, S. Strohm, H. J. Egelhaaf, A. Wadsworth, D. Baran, I. McCulloch, C. J. Brabec, *Adv. Energy Mater.* **2017**, *7*, 1701561.

[187] D. Bartesaghi, I. D. C. Pérez, J. Kniepert, S. Roland, M. Turbiez, D. Neher, L. J. A. Koster, *Nat. Commun.* **2015**, *6*, 7083.

[188] N. Gasparini, A. Wadsworth, M. Moser, D. Baran, I. McCulloch, C. J. Brabec, *Adv. Energy Mater.* **2018**, *8*, 1703298.

[189] P. Schilinsky, C. Waldauf, C. J. Brabec, *Appl. Phys. Lett.* **2002**, *81*, 3885.

[190] L. J. A. Koster, V. D. Mihailetchi, P. W. M. Blom, *Appl. Phys. Lett.* **2006**, *88*, 052104.

[191] S. R. Cowan, A. Roy, A. J. Heeger, *Phys. Rev. B* **2010**, *82*, 245207.

[192] S. A. Hawks, F. Deledalle, J. Yao, D. G. Rebois, G. Li, J. Nelson, Y. Yang, T. Kirchartz, J. R. Durrant, *Adv. Energy Mater.* **2013**, *3*, 1201.

[193] J. Gorenflot, A. Paulke, F. Piersimoni, J. Wolf, Z. Kan, F. Cruciani, A. El Labban, D. Neher, P. M. Beaujuge, F. Laquai, *Adv. Energy Mater.* **2018**, *8*, 1701678.

[194] S. Shoaee, A. Armin, M. Stolterfoht, S. M. Hosseini, J. Kurpiers, D. Neher, *Sol. RRL* **2019**, *3*, 1900184.

[195] M. M. Mandoc, F. B. Kooistra, J. C. Hummelen, B. De Boer, P. W. M. Blom, *Appl. Phys. Lett.* **2007**, *91*, 2005.

[196] L. J. A. Koster, V. D. Mihailetchi, R. Ramaker, P. W. M. Blom, *Appl. Phys. Lett.* **2005**, *86*, 123509.

[197] S. R. Cowan, W. L. Leong, N. Banerji, G. Dennler, A. J. Heeger, *Adv. Funct. Mater.* **2011**, *21*, 3083.

[198] T. M. Burke, S. Sweetnam, K. Vandewal, M. D. McGehee, *Adv. Energy Mater.* **2015**, *5*, 1500123.

[199] G. Dennler, M. C. Scharber, C. J. Brabec, *Adv. Mater.* **2009**, *21*, 1323.

[200] M. T. Dang, L. Hirsch, G. Wantz, *Adv. Mater.* **2011**, *23*, 3597.

[201] H. Zhang, X. Wang, L. Yang, S. Zhang, Y. Zhang, C. He, W. Ma, J. Hou, *Adv. Mater.* **2017**, *29*, 1703777.

[202] O. Inganäs, *Adv. Mater.* **2018**, *30*, 1800388.

[203] H. Zhou, Y. Zhang, J. Seifter, S. D. Collins, C. Luo, G. C. Bazan, T. Q. Nguyen, A. J. Heeger, *Adv. Mater.* **2013**, *25*, 1646.

[204] Y. Liang, Z. Xu, J. Xia, S. T. Tsai, Y. Wu, G. Li, C. Ray, L. Yu, *Adv. Mater.* **2010**, *22*, 135.

[205] J. Peet, J. Y. Kim, N. E. Coates, W. L. Ma, D. Moses, A J. Heeger, G. C. Bazan, *Nat. Mater.* **2007**, *6*, 497.

[206] X. Song, N. Gasparini, D. Baran, *Adv. Electron. Mater.* **2018**, *4*, 1700358.

[207] M. C. Heiber, T. Okubo, S. Ko, B. R. Luginbuhl, N. A. Ran, M. Wang, H. Wang, M. A. Uddin, H. Y. Woo, G. C. Bazan, T. Nguyen, *Energy Environ. Sci.* **2018**, *11*, 3019.

[208] J. Huang, J. H. Carpenter, C. Z. Li, J. S. Yu, H. Ade, A. K. Y. Jen, *Adv. Mater.* **2016**, *28*, 967.

[209] T. Liu, Z. Luo, Q. Fan, G. Zhang, L. Zhang, W. Gao, X. Guo, W. Ma, M. Zhang, C. Yang, Y. Li, H. Yan, *Energy Environ. Sci.* **2018**, *11*, 3275.

[210] Y. Xie, F. Yang, Y. Li, M. A. Uddin, P. Bi, *Adv. Mater.* **2018**, *1803045*, 1.

[211] N. Gasparini, L. Lucera, M. Salvador, M. Prosa, G. D. Spyropoulos, P. Kubis, H. J. Egelhaaf, C. J. Brabec, T. Ameri, *Energy Environ. Sci.* **2017**, *10*, 885.

[212] N. Gasparini, X. Jiao, T. Heumueller, D. Baran, G. J. Matt, S. Fladischer, E. Spiecker, H. Ade, C. J. Brabec, T. Ameri, *Nat. Energy* **2016**, *1*, 16118.

[213] L. Zhan, S. Li, T. Lau, Y. Cui, X. Lu, M. Shi, C. Z. Li, H. Li, J. Hou, H. Chen, *Energy Environ. Sci.* **2020**, DOI 10.1039/C9EE03710A.

[214] C. Sun, F. Pan, H. Bin, J. Zhang, L. Xue, B. Qiu, Z. Wei, Z. G. Zhang, Y. Li, *Nat. Commun.* **2018**, *9*, 1.

[215] Y. Wu, Y. Zheng, H. Yang, C. Sun, Y. Dong, C. Cui, H. Yan, Y. Li, *Sci. China Chem.* **2020**, *63*, 265.

[216] G. Simone, M. J. Dyson, S. C. J. Meskers, R. A. J. Janssen, G. H. Gelinck, *Adv. Funct. Mater.* **2019**, 1904205.

[217] R. D. Jansen-van Vuuren, A. Armin, A. K. Pandey, P. L. Burn, P. Meredith, *Adv. Mater.* **2016**, *28*, 4766.

[218] S. F. Tedde, J. Kern, T. Sterzl, J. Fürst, P. Lugli, O. Hayden, *Nano Lett.* **2009**, *9*, 980.

[219] I. K. Kim, X. Li, M. Ullah, P. E. Shaw, R. Wawrzinek, E. B. Namdas, S. C. Lo, *Adv. Mater.* **2015**, *27*, 6390.

[220] Y. L. Wu, N. Matsuhisa, P. Zalar, K. Fukuda, T. Yokota, T. Someya, *Adv. Electron. Mater.* **2018**, *1800311*, 1800311.

[221] M. Kielar, O. Dhez, G. Pecastaings, A. Curutchet, L. Hirsch, *Sci. Rep.* **2016**, *6*, 39201.

[222] W. Wang, F. Zhang, M. Du, L. Li, M. Zhang, K. Wang, Y. Wang, B. Hu, Y. Fang, J. Huang, *Nano Lett.* **2017**, *17*, 1995.

[223] Y. Fang, A. Armin, P. Meredith, J. Huang, *Nat. Photonics* **2019**, *13*, 1.

[224] Z. Wu, W. Yao, A. E. London, J. D. Azoulay, T. N. Ng, *Adv. Funct. Mater.* **2018**, *1800391*, 1.

[225] G. Simone, M. J. Dyson, C. H. L. Weijtens, S. C. J. Meskers, R. Coehoorn, R. A. J. Janssen, G. H. Gelinck, *Adv. Opt. Mater.* **2020**, *8*, https://doi.org/10.1002/adom.201901568.

[226] M. J. Dyson, M. Verhage, X. Ma, G. Simone, D. Tordera, R. A. J. Janssen, G. H. Gelinck, *Adv. Opt. Mater.* **2020**, *1901722*, https://doi.org/10.1002/adom.201901722.

[227] G. Simone, M. J. Dyson, S. C. J. Meskers, R. A. J. Janssen, G. H. Gelinck, *Adv. Funct. Mater.* **2019**, 1904205, https://doi.org/10.1002/adfm.201904205.

[228] T. Agostinelli, M. Campoy-Quiles, J. C. Blakesley, R. Speller, D. D. C. Bradley, J. Nelson, *Appl. Phys. Let..* **2008**, *93*, 203305.

[229] S. Yoon, J. Cho, K. M. Sim, J. Ha, D. S. Chung, *Appl. Phys. Lett.* **2017**, *110*, 083301.

[230] T. Rauch, M. Böberl, S. F. Tedde, J. Fürst, M. V. Kovalenko, G. Hesser, U. Lemmer, W. Heiss, O. Hayden, *Nat. Photonics* **2009**, *3*, 332.

[231] T. N. Ng, W. S. Wong, M. L. Chabinyc, S. Sambandan, R. A. Street, *Appl. Phys. Lett.* **2008**, *92*, 1.

[232] C. M. Benavides, S. Rechberger, E. Spiecker, M. Berlinghof, T. Unruh, M. Biele, O. Schmidt, C. J. Brabec, S. F. Tedde, *Org. Electron.* **2018**, *54*, 21-26.

[233] T. Yokota, P. Zalar, M. Kaltenbrunner, H. Jinno, N. Matsuhisa, H. Kitanosako, Y. Tachibana, W. Yukita, M. Koizumi, T. Someya, *Sci. Adv.* **2016**, *2*, e1501856.

[234] D. Han, Y. Khan, J. Ting, J. Zhu, C. Combe, A. Wadsworth, I. McCulloch, A. C. Arias, *Adv. Mater. Technol.* **2020**, 1901122, https://doi.org/10.1002/admt.201901122.

[235] J. Huang, J. Lee, J. Vollbrecht, V. V. Brus, A. L. Dixon, D. X. Cao, Z. Zhu, Z. Du, H. Wang, K. Cho, G. C. Bazan, T. Q. Nguyen, *Adv. Mater.* **2020**, *32*, 1906027.

[236] N. Strobel, N. Droseros, W. Köntges, M. Seiberlich, M. Pietsch, S. Schlisske, F. Lindheimer, R. R. Schröder, U. Lemmer, M. Pfannmöller, N. Banerji, G. Hernandez-Sosa, *Adv. Mater.* **2020**, *1908258*, https://doi.org/10.1002/adma.201908258.

[237] A. Armin, R. D. Jansen-Van Vuuren, N. Kopidakis, P. L. Burn, P. Meredith, *Nat. Commun.* **2015**, *6*, 1.

[238] B. Siegmund, A. Mischok, J. Benduhn, O. Zeika, S. Ullbrich, F. Nehm, M. Böhm, D. Spoltore, H. Fröb, C. Körner, K. Leo, K. Vandewal, *Nat. Commun.* **2017**, *8*, 15421.

[239] Z. Tang, Z. Ma, A. Sánchez-Díaz, S. Ullbrich, Y. Liu, B. Siegmund, A. Mischok, K. Leo, M. Campoy-Quiles, W. Li, K. Vandewal, *Adv. Mater.* **2017**, *29*, 1702184.

[240] A. Savateev, M. Antonietti, *ACS Catal.* **2018**, *8*, 9790.

[241] R. Li, J. Byun, W. Huang, C. Ayed, L. Wang, K. A. I. Zhang, *ACS Catal.* **2018**, *8*, 4735.

[242] A. Savateev, I. Ghosh, B. König, M. Antonietti, *Angew. Chemie Int. Ed.* **2018**, *57*, 15936.

[243] Y. Cao, W. Liu, J. Qian, T. Cao, J. Wang, W. Qin, *Chem. An Asian J.* **2019**, *14*, 2883.

[244] C. Chen, W. Ma, J. Zhao, *Chem. Soc. Rev.* **2010**, *39*, 4206.

[245] J. L. White, M. F. Baruch, J. E. Pander, Y. Hu, I. C. Fortmeyer, J. E. Park, T. Zhang, K. Liao, J. Gu, Y. Yan, T. W. Shaw, E. Abelev, A. B. Bocarsly, *Chem. Rev.* **2015**, *115*, 12888.

[246] S. Yang, W. Hu, X. Zhang, P. He, B. Pattengale, C. Liu, M. Cendejas, I. Hermans, X. Zhang, J. Zhang, J. Huang, *J. Am. Chem. Soc.* **2018**, *140*, 14614.

[247] J. Ran, J. Zhang, J. Yu, M. Jaroniec, S. Z. Qiao, *Chem. Soc. Rev.* **2014**, *43*, 7787.

[248] J. Kosco, M. Sachs, R. Godin, M. Kirkus, L. Francas, M. Bidwell, M. Qureshi, D. Anjum, J. R. Durrant, I. McCulloch, *Adv. Energy Mater.* **2018**, 1802181.

[249] J. Kosco, I. McCulloch, *ACS Energy Lett.* **2018**, *3*, 2846.

[250] F. Creutzig, P. Agoston, J. C. Goldschmidt, G. Luderer, G. Nemet, R. C. Pietzcker, *Nat. Energy* **2017**, *2*, 17140.

[251] S. Chen, T. Takata, K. Domen, *Nat. Rev. Mater.* **2017**, *2*, 17050.

[252] A. Fujishima, K. Honda, *Nature* **1972**, *238*, 37.

[253] Y. Goto, T. Hisatomi, Q. Wang, T. Higashi, K. Ishikiriyama, T. Maeda, Y. Sakata, S. Okunaka, H. Tokudome, M. Katayama, S. Akiyama, H. Nishiyama, Y. Inoue, T. Takewaki, T. Setoyama, T. Minegishi, T. Takata, T. Yamada, K. Domen, *Joule* **2018**, *2*, 509.

[254] X. Wang, K. Maeda, A. Thomas, K. Takanabe, G. Xin, J. M. Carlsson, K. Domen, M. Antonietti, *Nat. Mater.* **2009**, *8*, 76.

[255] G. Zhang, L. Lin, G. Li, Y. Zhang, A. Savateev, S. Zafeiratos, X. Wang, M. Antonietti, *Angew. Chemie Int. Ed.* **2018**, *57*, 9372.

[256] Y. Zheng, L. Lin, B. Wang, X. Wang, *Angew. Chemie Int. Ed.* **2015**, *54*, 12868.

[257] Q. Wang, T. Hisatomi, Y. Suzuki, Z. Pan, J. Seo, M. Katayama, T. Minegishi, H. Nishiyama, T. Takata, K. Seki, A. Kudo, T. Yamada, K. Domen, *J. Am. Chem. Soc.* **2017**, *139*, 1675.

[258] K. Maeda, K. Domen, *J. Phys. Chem. Lett.* **2010**, *1*, 2655.

[259] B. A. Pinaud, J. D. Benck, L. C. Seitz, A. J. Forman, Z. Chen, T. G. Deutsch, B. D. James, K. N. Baum, G. N. Baum, S. Ardo, H. Wang, E. Miller, T. F. Jaramillo, *Energy Environ. Sci.* **2013**, *6*, 1983.

[260] L. Bucher, N. Desbois, P. D. Harvey, G. D. Sharma, C. P. Gros, *Sol. RRL* **2017**, *1*, 1700127.

[261] S. Yanagida, A. Kabumoto, K. Mizumoto, C. Pac, K. Yoshino, *J. Chem. Soc. Chem. Commun.* **1985**, *0*, 474.

[262] R. S. Sprick, B. Bonillo, R. Clowes, P. Guiglion, N. J. Brownbill, B. J. Slater, F. Blanc, M. A. Zwijnenburg, D. J. Adams, A. I. Cooper, *Angew. Chemie Int. Ed.* **2016**, *55*, 1792.

[263] P. B. Pati, G. Damas, L. Tian, D. L. A. Fernandes, L. Zhang, I. B. Pehlivan, T. Edvinsson, C. M. Araujo, H. Tian, *Energy Environ. Sci.* **2017**, *10*, 1372.

[264] K. Landfester, R. Montenegro, U. Scherf, R. Güntner, U. Asawapirom, S. Patil, D. Neher, T. Kietzke, *Adv. Mater.* **2002**, *14*, 651.

[265] L. Li, Z. Cai, Q. Wu, W. Y. Lo, N. Zhang, L. X. Chen, L. Yu, *J. Am. Chem. Soc.* **2016**, *138*, 7681.

[266] C. Dai, S. Xu, W. Liu, X. Gong, M. Panahandeh-Fard, Z. Liu, D. Zhang, C. Xue, K. P. Loh, B. Liu, *Small* **2018**, *14*, 1801839.

[267] X. H. Zhang, X. P. Wang, J. Xiao, S. Y. Wang, D. K. Huang, X. Ding, Y. G. Xiang, H. Chen, *J. Catal.* **2017**, *350*, 64.

[268] X. Zong, X. Miao, S. Hua, L. An, X. Gao, W. Jiang, D. Qu, Z. Zhou, X. Liu, Z. Sun, *Appl. Catal. B Environ.* **2017**, *211*, 98.

[269] C. Dai, B. Liu, *Energy Environ. Sci.* **2019**, DOI 10.1039/c9ee01935a.

[270] J. Jayakumar, H. Chou, *ChemCatChem* **2020**, cctc. 201901725.

[271] J. Yang, D. Wang, H. Han, C. Li, *Acc. Chem. Res.* **2013**, *46*, 1900.

[272] X. Li, W. Bi, L. Zhang, S. Tao, W. Chu, Q. Zhang, Y. Luo, C. Wu, Y. Xie, *Adv. Mater.* **2016**, *28*, 2427.

[273] Z. Chen, S. Mitchell, E. Vorobyeva, R. K. Leary, R. Hauert, T. Furnival, Q. M. Ramasse, J. M. Thomas, P. A. Midgley, D. Dontsova, M. Antonietti, S. Pogodin, N. López, J. Pérez-Ramírez, *Adv. Funct. Mater.* **2017**, *27*, 1605785.

[274] G. Gao, Y. Jiao, E. R. Waclawik, A. Du, *J. Am. Chem. Soc.* **2016**, *138*, 6292.

[275] H. Yamashita, K. Mori, Y. Kuwahara, T. Kamegawa, M. Wen, P. Verma, M. Che, *Chem. Soc. Rev.* **2018**, *47*, 8072.

[276] A. Rodenberg, M. Orazietti, B. Probst, C. Bachmann, R. Alberto, K. K. Baldridge, P. Hamm, *Inorg. Chem.* **2015**, *54*, 646.

[277] A. Reynal, F. Lakadamyali, M. A. Gross, E. Reisner, J. R. Durrant, *Energy Environ. Sci.* **2013**, *6*, 3291.

[278] E. Pastor, F. Le Formal, M. T. Mayer, S. D. Tilley, L. Francàs, C. A. Mesa, M. Grätzel, J. R. Durrant, *Nat. Commun.* **2017**, *8*, 1.

[279] A. Liu, C. W. Tai, K. Holá, H. Tian, *J. Mater. Chem. A* **2019**, *7*, 4797.

[280] L. Wang, R. Fernández-Terán, L. Zhang, D. L. A. Fernandes, L. Tian, H. Chen, H. Tian, *Angew. Chem. Int. Ed.* **2016**, *55*, 12306-12310.

[281] L. Feng, C. Zhu, H. Yuan, L. Liu, F. Lv, S. Wang, *Chem. Soc. Rev.* **2013**, *42*, 6620.

[282] X. Wang, K. Maeda, X. Chen, K. Takanabe, K. Domen, Y. Hou, X. Fu, M. Antonietti, *J. Am. Chem. Soc.* **2009**, *131*, 1680.

[283] C. M. Aitchison, R. S. Sprick, A. I. Cooper, *J. Mater. Chem. A* **2019**, *7*, 2490.

[284] X. Wang, L. Chen, S. Y. Chong, M. A. Little, Y. Wu, W. H. Zhu, R. Clowes, Y. Yan, M. A. Zwijnenburg, R. S. Sprick, A. I. Cooper, *Nat. Chem.* **2018**, *10*, 1180.

[285] V. S. Vyas, F. Haase, L. Stegbauer, G. Savasci, F. Podjaski, C. Ochsenfeld, B. V. Lotsch, *Nat. Commun.* **2015**, *6*, 8508.

[286] T. Banerjee, K. Gottschling, G. Savasci, C. Ochsenfeld, B. V. Lotsch, *ACS Energy Lett.* **2018**, *3*, 400.

[287] Z. Hu, Z. Wang, X. Zhang, H. Tang, X. Liu, F. Huang, Y. Cao, *iScience* **2019**, *13*, 33.

[288] X. Zhang, T. Peng, S. Song, *J. Mater. Chem. A* **2016**, *4*, 2365.

[289] K. Takanabe, K. Kamata, X. Wang, M. Antonietti, J. Kubota, K. Domen, *Phys. Chem. Chem. Phys.* **2010**, *12*, 13020.

[290] X. Zhang, F. Shen, Z. Hu, Y. Wu, H. Tang, J. Jia, X. Wang, F. Huang, Y. Cao, *ACS Sustain. Chem. Eng.* **2019**, *7*, 4128.

[291] S. Hornig, T. Heinze, C. R. Becer, U. S. Schubert, W. Devonport, T. P. T. Le, R. T. A. Mayadunne, G. F. Meijs, C. L. Moad, G. Moad, E. Rizzardo, S. H. Thang, *J. Mater. Chem.* **2009**, *19*, 3838.

[292] K. Landfester, *Adv. Mater.* **2001**, *13*, 765.

[293] S. Rajasekar, P. Fortin, V. Tiwari, U. Srivastva, A. Sharma, S. Holdcroft, *Synth. Met.* **2019**, *247*, 10.

The development of the bulk heterojunction, in terms of materials design, device engineering, and the underpinning physical understanding, has led to significant improvements in organic photovoltaics. Looking forward, the bulk heterojunction concept is likely to allow even greater solar cell efficiencies and interestingly, can be applied to other organic electronic applications, such as organic photodetectors and photocatalysts.

Keyword bulk heterojunction

Andrew Wadsworth*, Zeinab Hamid, Jan Kosco, Nicola Gasparini, Iain McCulloch*

The Bulk Heterojunction in Organic Photovoltaic, Photodetector and Photocatalytic Applications